Available online at www.sciencedirect.com
ScienceDirect
Combustion and Flame 153 (2008) 288–315
Combustion and Flame
www.elsevier.com/locate/combustflame

Experimental and numerical analysis of stratified turbulent V-shaped flames

Vincent Robin [a], Arnaud Mura [a,*], Michel Champion [a], Olivier Degardin [b], Bruno Renou [b], Mourad Boukhalfa [b]

[a] *LCD, ENSMA, UPR9028 CNRS, Poitiers, France*
[b] *Coria, INSA de Rouen, UMR6614, Rouen, France*

Received 10 May 2007; received in revised form 16 September 2007; accepted 23 October 2007

Available online 26 December 2007

Abstract

The present paper is devoted to (i) the experimental study of partially premixed combustion with strong equivalence ratio gradients, i.e., stratification of the reactive mixture and (ii) the numerical modeling of turbulent reactive flows in such situations where reactants are far from being ideally premixed. From a practical point of view, at least two variables are necessary to describe the local thermochemistry in this case: the mixture fraction ξ and the fuel mass fraction Y_f are considered to represent respectively the local composition of the fresh mixture and the progress of chemical reactions. From the experimental point of view, the use of simultaneous imaging techniques allows the evaluation of both variables in terms of fuel mole fraction and temperature. In the present study, a combined acetone PLIF measurement and Rayleigh scattering technique is used. The influence of temperature on the fluorescence signal is corrected thanks to the knowledge of the local temperature through Rayleigh scattering measurements. Conversely, the influence of the acetone Rayleigh cross section can be evaluated with the local value of acetone mole fraction. Using the iterative procedure already described by Degardin et al. [Exp. Fluids 40 (2006) 452–463], the corrected fuel mole fraction and temperature fields can be obtained. Here the particular flow configuration under study is a stratified turbulent V-shaped flame of methane and air. In a first step of the analysis, the optical diagnostics are used to perform a detailed investigation of the flame thickness with a special emphasis on the influence of partially premixed conditions. In a second step, experimental data are used to evaluate the LW-P model as defined by Robin et al. [Combust. Sci. Technol. 178 (10–11) (2006) 1843–1870] to calculate turbulent reactive flows with partially premixed conditions based on an earlier analysis by Libby and Williams [Combust. Sci. Technol. 161 (2000) 351–390]. The closure problem raised by the mean scalar dissipation terms is also discussed in the light of experimental results. Since the usual closures for nonreactive flows are expected to be unsuitable to describe reactive scalar fluctuations decay a new modeling proposal based on the recent developments of Mura et al. [Combust. Flame 149 (2007) 217–224] is used. After a preliminary validation step where numerical predictions of the flame mean quantities are compared successfully with the experimental database, numerical simulations are used to describe the mean structure of stratified flames and in particular the evolution of the mean chemical reaction rate for different partially premixed conditions.

* Corresponding author. Fax: +33 (0) 5 49 49 81 76.
E-mail address: arnaud.mura@lcd.ensma.fr (A. Mura).

0010-2180/$ – see front matter
doi:10.1016/j.combustflame.2007.10.008

Keywords: Turbulent combustion; Partially premixed combustion; Stratified flames; Flame thickness; Mean scalar dissipation

1. Introduction

In many practical situations relevant to working conditions in energy conversion devices, from internal combustion engines to industrial furnaces, turbulent mixing of fuel and air prior to combustion leads to a reactive mixture that is not homogeneous. Accordingly the equivalence ratio of the mixture is variable in space and time and combustion occurs under partially premixed conditions. Depending on the fuel–air distribution or on the corresponding shape of the probability density function (PDF) of the equivalence ratio with respect to stoichiometric conditions, two different situations are expected:
(i) The first situation concerns the case where the fuel–air mixtures remain either lean or rich everywhere in such a manner that no diffusion flame can exist. This particular situation is commonly referred to as stratified combustion.
(ii) The second situation is a more general and complex situation, where the spatial distribution of equivalence ratio leads to the coexistence of fuel-rich and -lean heterogeneities, giving rise to a combination of premixed and diffusion modes. In some circumstances, the resulting reaction zone can be described as a staggered combustion with a *primary stage* corresponding to a premixed combustion zone (but with different local equivalence ratio depending on the location considered along the flame front), followed by a *secondary stage* corresponding to various multiple diffusion flames.

Various experimental and numerical studies have been carried out to evaluate the influence of spatial or temporal variations of the equivalence ratio and these for different geometrical and initial conditions. The most noticeable effects that have been evidenced can be summarized as follows: (i) extension of the flammability limits, (ii) modification of the inner structure of the flame, and (iii) strong dependence of the combustion efficiency on both turbulence and scalar length scales.

The concept of flammability limit is directly related to the propagative nature of a premixed flame front and especially to the value of the laminar flame speed. The chemical and physical mechanisms that drive the flame propagation into a medium with large and small scales fuel–air heterogeneities are rather different from those observed for homogeneous flames, as evidenced by previous experimental [1–3] and numerical studies [4,5].

For instance, if we first consider large-scale stratification of the equivalence ratio, flame fronts have been found to be able to propagate from stoichiometric conditions to extremely lean mixtures with a flame speed that can be 20% and up to 30% higher than the propagation velocity in the corresponding homogeneous mixture at the same mean equivalence ratio. This behavior is related to the history of the combustion process: flame propagation is back-supported by heat and radicals flux resulting from combustion that has occurred at a higher equivalence ratio. Accordingly, the knowledge of the local value of the equivalence ratio is clearly not sufficient to explain the differences between stratified and homogeneous combustion since all the previous events in the combustion process must be taken into account: those phenomena are related to some kind of memory effects of the flame. Of course, since these are nonlocal effects, they are extremely difficult to incorporate into turbulent combustion models.

The instantaneous structure of partially premixed flame fronts in terms of flame wrinkling, curvature, and rate of strain is also influenced by local fuel heterogeneities. These effects have been already studied and sometimes opposite trends have been found [6–9]. Nevertheless, fuel–air heterogeneities are expected to enhance flame wrinkling, at least when the turbulent intensity is not too large with respect to typical values of the laminar flamelet propagation velocity [10] and when the typical length scale attached to the equivalence ratio is smaller than the integral turbulent length scale.

Indeed, flame wrinkling is the result of both turbulence and fuel–air heterogeneities. In the case of freely propagating homogeneous flames, the experiments performed by Renou et al. [11] have shown that flame curvature statistics are strongly influenced by the integral turbulent length scale. For stratified flames, equivalence ratio fluctuations are other sources of local variations for the reaction rate since local flame fronts propagate with different displacement speeds. This effect that leads to additional deformation of the flame front can play a substantial role when the scale of fuel–air heterogeneities is smaller than the scale of turbulence as long as the ratio u'/S_{L}^{0} is not too large. If this latter situation does not hold, turbulence is expected to prevail against laminar propagation.

This strong coupling between turbulence and stratification can be also studied in terms of combustion efficiency by considering some kind of global mean reaction rate. The evaluation and understanding of this coupling, for different conditions, have been the objective of previous experimental and numeri-

Nomenclature

A	slope of the equilibrium line in (ξ, Y_f) space
A_n	grid turbulence decay coefficient
B	pre-exponential factor
B_n	grid turbulence decay coefficient
C_μ	modeling constant $C_\mu = 0.09$
C_0	calibration factor (PLIF signal)
C_1	calibration factor (Rayleigh signal)
D	molecular diffusivity of chemical species
dV_c	detection volume
$\mathcal{D}$	domain of definition of the PDF
I_0	incident laser light intensity
k	turbulence kinetic energy
k_B	Boltzmann constant
K	strain rate (e.g., K_{PP} strain rate induced by partial premixing)
Ka	Karlovitz number
L_T	integral length scale of turbulence
L_ξ	integral length scale of scalar ξ fluctuations
L_Φ	integral length scale of scalar equivalence ratio fluctuations
m	grid turbulence decay exponent
M	mesh size (grid of turbulence)
n	grid turbulence decay exponent
N	total molecular number density
p	slope of the fluctuations line $p = \overline{\rho\xi'' Y_f''}/\overline{\rho\xi''^2}$
P	total pressure
$\tilde{P}$	Favre average PDF
$\tilde{P}_1$	conditional Favre average PDF at $\xi = \xi_1$
$\tilde{P}_2$	conditional Favre average PDF at $\xi = \xi_2$
R_{Y_f}	scalar to turbulence time scales ratio $R_{Y_f} = \tau_{Y_f}/\tau_T$
R_ξ	scalar to turbulence time scales ratio $R_\xi = \tau_\xi/\tau_T$
$R_{Y_f\xi}$	scalar to turbulence time scales ratio $R_{Y_f\xi} = \tau_{Y_f\xi}/\tau_T$
Re_T	turbulent Reynolds number $Re_T = u' L_T/\nu$
Re_λ	Reynolds number based on Taylor length scale $Re_\lambda = u'\lambda/\nu$
S	segregation rate
S_F	signal of fluorescence
S_R	Rayleigh scattering signal
Sc_T	turbulent Schmidt number ($Sc_T = 0.7$)
S_L^0	propagation velocity of the planar unstrained laminar premixed flame
t	time
T	temperature
T_a	temperature of activation
T_i	inner layer temperature
T_0	temperature under standard conditions ($T_0 = 298$ K)
T^*	ratio of temperature and molecular weight $T^* = T/W$
U	exit velocity based on mass flow rate
u_k	velocity component
w	local propagation velocity inside the turbulent flame brush
W	molecular weight of the mixture
x, y, z	coordinates in Cartesian reference
Y	mass fraction of a chemical species
z_0	virtual origin (grid turbulence decay law)

Greek symbols

α, β, γ	parameters of the PDF shape
δ_L	instantaneous flame thickness
δ_L^0	flame thickness of reference (planar unstrained laminar premixed flame)
ϵ	dissipation rate of turbulence kinetic energy k
ϵ_{Y_f}	dissipation rate of scalar variance $\widetilde{Y_f''^2}$
ϵ_ξ	dissipation rate of scalar variance $\widetilde{\xi''^2}$
$\epsilon_{Y_f\xi}$	dissipation rate of cross scalar correlation $\widetilde{Y_f''\xi''}$
η_{opt}	overall efficiency of collection optics
λ	Taylor length scale (or wavelength)
ν	molecular viscosity
ξ	mixture fraction
ρ	density of the mixture
σ	molecular absorption cross-section
τ_T	turbulent integral time scale $\tau_T = k/\epsilon$
τ_{Y_f}	scalar mixing integral time scale $\tau_{Y_f} = \widetilde{Y_f''^2}/\tilde{\epsilon}_{Y_f}$
τ_ξ	scalar mixing integral time scale $\tau_\xi = \widetilde{\xi''^2}/\tilde{\epsilon}_\xi$
$\tau_{Y_f\xi}$	scalar mixing integral time scale $\tau_{Y_f\xi} = \widetilde{Y_f''\xi''}/\tilde{\epsilon}_{Y_f\xi}$
τ_{chem}	chemical time scale
ϕ	diameter of gas cooker injector (p. 10)
Φ	equivalence ratio
Ψ	fluorescence quantum yield
χ_i	mole fraction of species i
ω	chemical production rate

Subscripts

f	fuel
H	homogeneous conditions
k	direction in Cartesian reference
L	refers to laminar conditions
NR	reactive (or flamelet) contribution
R	nonreactive (nonflamelet) contribution
rod	value at stabilizing rod location
PP	refers to partially premixed conditions
S	stratified conditions
st	stoichiometric conditions
T	refers to turbulent conditions

Superscripts

$'$	fluctuations with respect to Reynolds average
$''$	fluctuations with respect to Favre average
0	planar and unstrained
max	maximum value
min	minimum value
air	value in air

Others

∇q	gradient of quantity q
$\|\boldsymbol{q}\|$	norm of vector $\boldsymbol{q}$
$\overline{q}$	Reynolds average of quantity q
$\tilde{q}$	Favre average of quantity q
$\langle q \rangle$	expectation or mean value as obtained from experiments

cal studies [7,8,12–14]. No clear conclusion has been drawn from these results, as the influence of fuel–air heterogeneities has been found to either enhance or reduce combustion efficiency. The distribution of fuel–air fluctuations respective to the value of mixture fraction at stoichiometric conditions, as well as the strong nonlinearity of the reaction rate, may explain such different behavior [13].

As far as possible, these characteristics must be taken into account when developing numerical models to deal with such partially premixed flames. In this respect the model proposed by Libby and Williams (LW) offers an efficient way to evaluate the mean chemical rate, as it is based on a two-scalars PDF and takes finite-rate chemistry into account [15]. Clearly, under the partially premixed conditions under study, combustion phenomena can occur locally in mixtures close to flammability limits, so that the notion of "thickened flamelets," viz., involving effects of finite-rate chemistry, applies. Accordingly, the characteristic Damkhöler number cannot always be considered as infinite and effects of finite-rate chemistry may no longer be negligible. The Libby–Williams approach has already demonstrated its ability to recover not only the flamelet regime of turbulent combustion but also the thickened flame regime, at least for fully premixed situations [16]. Here the generalized form of the LW model introduced by Robin et al. [17] for partially premixed conditions is used. It will be denoted by LW-P (Libby–Williams-Poitiers) in the following. In this latter model the closure relies on a presumed joint scalar PDF made of four Dirac delta functions. This allows the removal from the original LW model of one constraint that may be crucial in some circumstances [17], namely that the cross scalar correlation is directly connected to the product of the two variances and then keeps the same sign throughout the reactive flow, a feature in disagreement with a detailed analysis of the local structure of the flame in some situations. However, the quantitative importance of this feature depends clearly on the flow investigated as well as the region of the flow considered.

In the present study turbulent partially premixed combustion is studied in the special case where a strong mean gradient of equivalence ratio exists at large scales. The studied particular flow configuration is a stratified turbulent V-shaped flame of methane and air, as already investigated experimentally by Degardin et al. [18]. In this reference, the joint dynamics of mixture fraction and temperature dynamics is studied thanks to a simultaneous acetone PLIF (planar laser-induced fluorescence) and Rayleigh scattering technique. Different equivalence ratio gradients are considered from $\langle \Phi \rangle = 0.8$ or $\langle \Phi \rangle = 1.2$ at the center of the wind tunnel exit to $\Phi = 0$ at the periphery.

The paper is organized as follows: after a general presentation of the experimental setup, the experimental results are used to perform a detailed analysis of the flame front structure in terms of flame thickness and curvature. In a second step, the experimental database is used to test the ability of the LW-P model to deal with the so-called stratified conditions. In fact, the model has already demonstrated its ability to represent partially premixed combustion [17] but not with such a strong mean gradient of equivalence ratio. The problem raised by the closure of the scalar dissipation terms in such situations is also discussed. After this preliminary and successful validation step, numerical results are used to gather informations on how the flame brush structure is modified by equivalence ratio heterogeneities. The numerical results associated with a detailed analysis of the experimental database provide new insights into turbulent combustion in partially premixed situations.

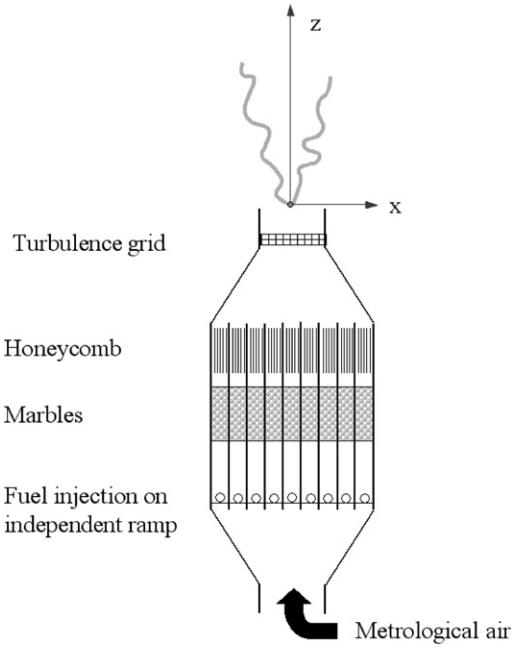

Fig. 1. Experimental setup.

2. Experimental setup and optical diagnostics

2.1. Experimental setup

The experimental setup consists of a vertical wind tunnel where turbulent flames are stabilized on a 0.8-mm-diameter heated rod positioned at the center of a combustion chamber ($x = 0$ mm, $z = 0$ mm) with an 80×80 mm square section; see Fig. 1. This setup is similar to the one already used by Degardin et al. [18] to study laminar flames. The air-flow rate of 86 Nm^3/h is filtered by high-efficiency filters (filtering efficiency more than 99.99% for 0.1 μm particles) to avoid Mie scattering of small particles, and this flow is directed into an upstream mixing chamber made of nine parallel vertical compartments. Thanks to these compartments, which can carry mixtures with different stoichiometries, it is possible to produce an upstream stratified flow with a transverse gradient of equivalence ratio. Each compartment is made of 13 gas cooker injectors (with diameter $\phi = 0.62$ mm) situated on the injection ramp. The free jets of gas are then mixed with air and the resulting flow is homogenized thanks to small glass marbles. The flow is then laminarized with a honeycomb structure and conducted to the study zone through a convergent channel. Accordingly, different stratified conditions can be obtained and used to characterize the influence of large- and small-scale fuel heterogeneities on both laminar and turbulent flames. Two-dimensional symmetrical profiles of equivalence ratio are generated in

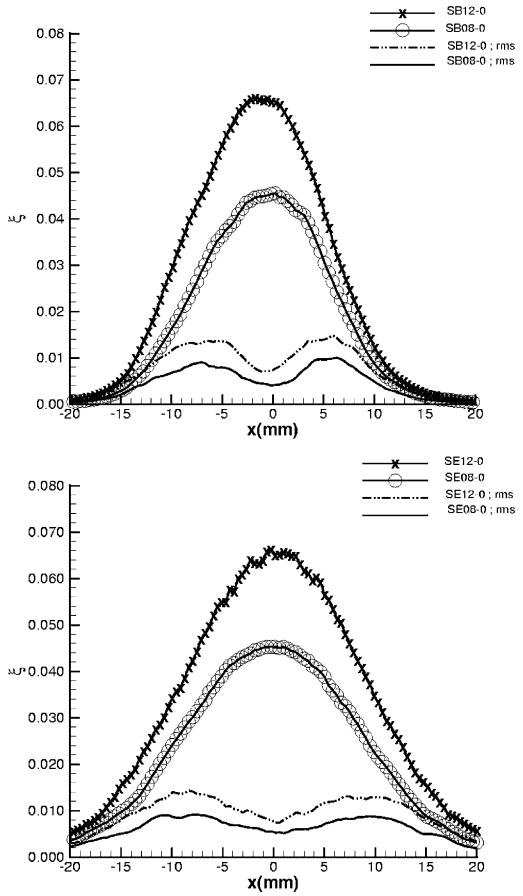

Fig. 2. Mean and RMS mixture fraction profiles without combustion at $z = 20$ mm. Grids of turbulence are B (top) or E (bottom). Measurements are performed with PLIF on acetone.

the mixing chamber with a maximum at the central axis ($x = 0$). On both sides of this axis, the equivalence ratio decreases continuously; see Fig. 2. Two different turbulence grids, called grid B and grid E, can be added at the exit of the convergent, 70 mm upstream of the stabilizing rod (i.e., $z = -70$ mm). The stratified cases are referenced in terms of the turbulence grid used, the amplitude of the equivalence ratio difference from the center of the wind tunnel Φ_{rod} to the value at the periphery Φ_{min}, for instance, SE08-0 for a stratified mixture obtained with turbulence grid B and with an equivalence ratio that decreases from 0.8 at the center of the wind tunnel exit to 0 at the periphery. Conditions are summarized in Table 1. The study zone corresponds to distances ranging from $z = 20$ to $z = 100$ mm downstream of the turbulence-generating grid. The nonreactive turbulent flow structure in the wind tunnel has been characterized using laser Doppler velocimetry (LDV) in a former study [19]. From this previous analysis, it

Table 1
Conditions of stratification in terms of equivalence ratio value (mixture fraction value, respectively) at the center of the wind tunnel and at the periphery

Name	Cases	Turb. grid	$\Phi(\xi)$	$\Phi_{\text{rod}}(\xi_{\text{rod}})$	$\Phi_{\text{min}}(\xi_{\text{min}})$	Numerical test
HB06	Homogeneous	B	0.6 (0.034)	–	–	
HB07	Homogeneous	B	0.7 (0.039)	–	–	
HE05	Homogeneous	E	0.55 (0.031)	–	–	
HE06	Homogeneous	E	0.6 (0.034)	–	–	X
SB08-0	Stratified	B	–	0.8 (0.045)	0	X
SB12-0	Stratified	B	–	1.2 (0.065)	0	X
SE08-0	Stratified	E	–	0.8 (0.045)	0	
SE10-0	Stratified	E	–	1.0 (0.055)	0	X
SE12-0	Stratified	E	–	1.2 (0.065)	0	

Notes. Typical profiles of mean and fluctuations levels of mixture fraction are reported in Fig. 2. In the table, Φ_{rod} and Φ_{min} denotes the values of equivalence ratio at the stabilization point (at rod location) and at the periphery, respectively.

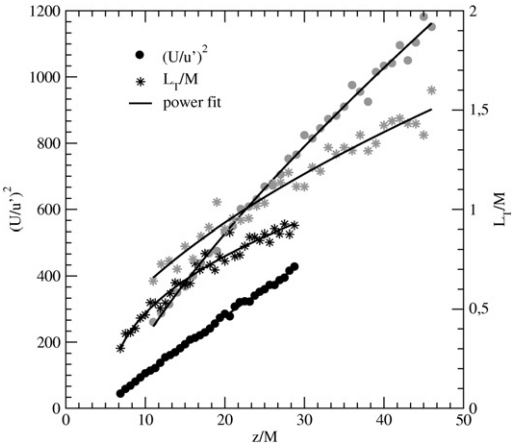

Fig. 3. Integral length scale and fluctuating velocity evolution as a function of z/M for grid B (gray) and grid E (black). The mesh size of the grid is $M = 5$ mm for grid B and $M = 8$ mm for grid E.

is concluded that (i) the boundary layers induced by the walls are very thin and do not influence the flame structure, and (ii) turbulence can be considered as homogeneous and isotropic. Temporal correlation coefficients have been obtained from the LDV signals in the centerline (i.e., $x = y = 0$) for various values of z. Using the Taylor approximation, the integral length scale based on the longitudinal velocity component can be deduced from the integral time scale and the mean axial velocity, as shown in Fig. 3. Those integral length scales and the fluctuating velocity are related to the axial position z according to power laws as

$$\frac{u'^2}{U^2} = A_n \left(\frac{z}{M} - \frac{z_0}{M} \right)^n, \tag{1}$$

$$\frac{L_{\text{T}}}{M} = B_m \left(\frac{z}{M} - \frac{z_0}{M} \right)^m. \tag{2}$$

Flow conditions are summarized in Table 2.

Table 2
Averaged flow conditions in the study zone $z = 0$ mm to 100 mm

	Grid B	Grid E
U (m/s)	3.75	3.14
u' (m/s)	0.139	0.237
u'/U (%)	3.7	7.5
L_{T} (mm)	5.5	6.1
λ (mm)	2.9	2.4
Re_{T}	53	101
Re_{λ}	29	39
z_0/M	4	4.5
A	46.93	16.2
B	0.268	0.273
m	0.459	0.419
n	0.86	1.01

Notes. U is the mean velocity, u' the velocity RMS, L_{T} the integral length scale, λ the Taylor scale obtained from the osculating parabola of the autocorrelation coefficient, τ_{T} the eddy-turnover-time L_{T}/u', $\text{Re}_{\text{T}} = u' L_{\text{T}}/\nu$ the turbulent Reynolds number, $\text{Re}_{\lambda} = u'\lambda/\nu$ the Reynolds number based on the Taylor length scale and z_0/M, and A, B, m, and n the coefficients of the power laws (see Eqs. (1) and (2)).

2.2. Optical diagnostics

In order to point out the influence of small- and large-scale fuel heterogeneities on the flame behavior and to make comparisons with numerical models easier, velocity, temperature, and mixture fraction fields need to be measured. The velocity field is obtained using a particle image velocimetry (PIV) cross-correlation technique. A laser sheet with a thickness of 0.6 mm is obtained with a Nd:YAG laser (Big Sky laser, 120 mJ/pulse). The flow is seeded with ZrO_2 particles and the scattered light is collected by a CCD camera (FlowMaster LaVision, 12 bits, 1280 × 1024 pixels) with a 50-mm Nikkon lens (f:1/1.2), giving a magnification ratio of 23.5 pixels/mm. The PIV algorithm is taken from the standard commercial package

available in Davis 6.2 (LaVision) and relies on the method proposed by Scarano and Reithmuller [20]. This is a multipass algorithm with an adaptive window deformation. The initial size of the interrogation window is $(64)^2$ pixels and six iterations are used to obtain a final interrogation window whose size is $(32)^2$ pixels, with an overlap of 50%. In the present study, a method based on simultaneous measurements of temperature and fuel mole fraction by Rayleigh scattering and PLIF on acetone is used. Details on the accuracy and limits of this technique have been already reported by Degardin et al. [18]. A brief presentation of the methodology is given below.

2.2.1. Acetone PLIF

For weak excitation, the fluorescence signal S_F from acetone molecule is given by

$$S_F(x,y) = I_0(x,y,\lambda) dV_c \eta_{opt} \left[\frac{\chi_{Acetone}(x,y) P}{k_B T}\right] \times \sigma(\lambda,T)\Psi\left(\lambda, T, P, \sum_i \chi_i\right), \quad (3)$$

where $I_0(\lambda)$ is the local laser energy density in the detection volume dV_c [cm^3], and η_{opt} is the overall efficiency of the collection optics. The bracketed term is the acetone number density [cm^{-3}], given as the product of mole fraction $\chi_{Acetone}$ and total pressure P divided by $k_B T$, where k_B is the Boltzmann constant and T the temperature. The final two quantities are σ, the molecular absorption cross section of the tracer [cm^2], and the fluorescence quantum yield Ψ. The effect of composition variations on the fluorescence quantum yield can be neglected and, for constant pressure and a fixed wavelength excitation, the fluorescence signal given by Eq. (3) becomes

$$S_F(x,y) = C_0(x,y)\left[\frac{\chi_{Acetone}(x,y)}{T(x,y)}\right] \times \sigma(\lambda,T)\Psi(\lambda,T) \quad (4)$$

or

$$S_F(x,y) = C_0(x,y)\chi_{Acetone}(x,y) g(\lambda,T),$$

where $C_0(x,y)$ is a calibration factor and $g(\lambda,T) = \sigma(\lambda,T)\Psi(\lambda,T)/T(x,y)$. Based on an experimental study at atmospheric pressure, Thurber and Hanson [21] have evaluated the temperature influence on the different terms of this function $g(\lambda,T)$. Tabulated values of the ratio $g(\lambda,T)/g(\lambda,T_0)$ have been reported and indicate how the temperature decreases the fluorescence signal per unit mole fraction [21]. $T_0 = 298$ K is the temperature in standard conditions.

Using acetone as a tracer in combustion studies requires special care. Acetone must be a good fuel tracer in order to validate the assumption that acetone mole fraction measured by PLIF is linearly related to the fuel mole fraction. As a consequence, acetone influence on methane–air flame structure must be negligible, and acetone decomposition must be approximately the same as methane decomposition. In addition, acetone and fuel mass diffusivities need to be similar as it is the case when considering pure methane. Consequently a 5% seeding, as the volume of acetone in methane, has been fixed to optimize the fluorescence signal while minimizing the impact of acetone on methane combustion. For stoichiometric conditions this corresponds to a 0.1% seeding volume of acetone into the fresh mixture.

2.2.2. Rayleigh scattering technique

The Rayleigh scattering technique is based on an elastic interaction between an incident laser light and gas molecules. For a flow containing different chemical species, the Rayleigh scattering signal is given by

$$S_R(x,y) = I_0(x,y,\lambda) C_1 N(x,y) \sum_i \chi_i(x,y)\left(\frac{\partial\sigma_R}{\partial\Omega}\right)_i, \quad (5)$$

where $I_0(\lambda)$ is the incident laser light intensity. C_1 is the system calibration constant, which accounts for the optical collection efficiency and characteristic lengths of the laser sheet imaged on the detector. N is the total molecular number density and χ_i the mole fraction of the different species. $(\partial\sigma_R/\partial\Omega)_i$ is the Rayleigh scattering cross section for molecules i. Assuming constant pressure conditions and using the ideal gas law, the total molecular number density is a function of temperature only. Accordingly, Eq. (5) becomes

$$S_R(x,y) = C_1 \frac{1}{T(x,y)} \sum_i \chi_i(x,y)\left(\frac{\partial\sigma_R}{\partial\Omega}\right)_i. \quad (6)$$

Recent results obtained with this technique applied to a turbulent V-shaped flame have been reported by Knaus et al. [22].

2.2.3. Simultaneous measurements

Applying these techniques separately to the case of partially premixed combustion raises some important questions. First, the LIF signal decreases strongly with temperature through the function $g(\lambda,T)$. The distance needed for temperature to increase from the fresh gas temperature (300 K) to the acetone pyrolysis temperature (1000 K) may not be negligible, especially for lean homogeneous or stratified mixtures. Moreover, if acetone is locally present in the mixture for PLIF acetone measurements, a contribution of the Rayleigh scattering of acetone molecules to the

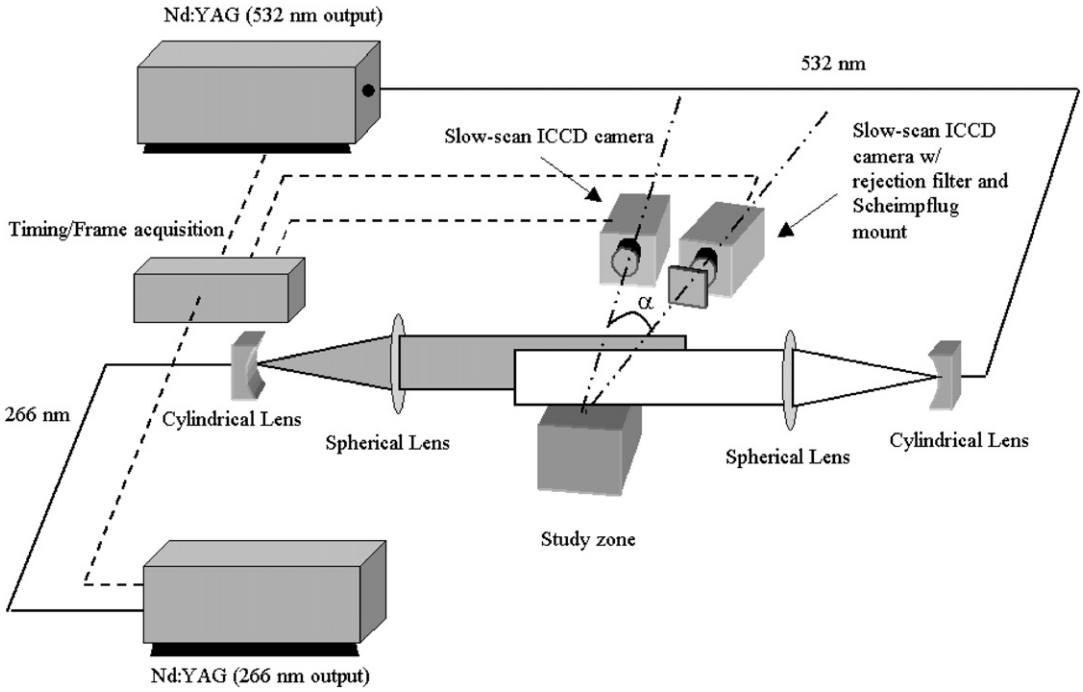

Fig. 4. The optical setup used for the simultaneous planar laser-induced fluorescence on acetone and Rayleigh scattering showing the camera arrangement and the sheet for the 266-nm and 532-nm laser beams.

temperature field can be observed, even for very low concentrations of acetone.

With simultaneous measurements by Rayleigh scattering and acetone PLIF, the influence of temperature on fuel mole fraction measurements and the contribution of acetone Rayleigh cross-section on temperature measurements can be corrected [18]. Moreover, the fluorescence signal-to-noise ratio (SNR) strongly decreases with temperature and the accuracy of the corrected value of the fuel mole fraction decreases. In such conditions, the SNR correction of the fluorescence signal is limited to $T = 500$ K. The contribution of this iterative correction on the local methane mole fraction and its gradient has been evaluated and appears to increase strongly with temperature, reaching a relative equivalence ratio difference of more than 50% at the isotherm 500 K, as shown by Degardin et al. [18].

2.3. Optical apparatus

The optical arrangement used for the simultaneous measurement of temperature and fuel mole fraction by Rayleigh scattering coupled to acetone PLIF is presented in Fig. 4. A frequency-doubled Nd-YAG laser with a typical energy of 400 mJ/pulse is used for the Rayleigh scattering technique. Thanks to planoconcave cylindrical lenses (nominal focal lengths $f = 20$ mm and $f = 200$ mm) and a plano-convex spherical lens (nominal focal length $f = 1000$ mm), a laser sheet of constant thickness and height is obtained in the study zone. The laser sheet properties (thickness and shape) are characterized using a CCD camera (WincamD 14 bits) coupled to attenuator filters. The laser sheet thickness is found to be constant and equal to 100 μm in the study zone. The Rayleigh scattering signal is collected with a PI-MAX2:512 intensified CCD camera with a 512 × 512 pixel array, fiber-optically coupled to a GEN III (UNIGEN coating) intensifier. The images are digitized with a 16-bit precision. Using a 50-mm Nikkon lens (f/1.2) and an extension tube of 18 mm, a magnification ratio of 20.2 pixels/mm is obtained. The intensifier is gated at 100 ns, which is necessary to fully capture the whole laser pulse of 6 ns, but short enough to suppress most of the flame chemiluminescence. For the PLIF technique, a single Nd:YAG laser internally quadrupled to produce a 266-nm laser beam with a typical pulse energy of 60 mJ/pulse is used to excite acetone molecules. The acetone fluorescence signal is recorded with a PI-MAX:512 intensified CCD camera with a 512 × 512 pixel array, fiber-optically coupled to a GEN II intensifier. Using a 50-mm Nikkon lens (f/1.2) and an extension tube of 12 mm, a magnification ratio of 12.9 pixel/mm is obtained. The intensifier is gated at 100 ns and the signal is filtered by a 532-nm rejection filter to suppress the Rayleigh scattering signal and its background reflec-

tions. The 532-nm and 266-nm beams are steered to opposite sides of the wind tunnel and pass through the centerline $x = 0$ of the study zone. The two laser sheets are effectively superimposed using a perforated plate with three thin holes ($\phi = 1$ mm). As these holes are perfectly lined up along the central axis, the laser sheets can be superimposed with an accuracy of 0.5 mm. In order to decrease the reflection noise level for Rayleigh scattering measurements, the two ICCD cameras have been located on the same side of the laser sheets. The ICCD camera for Rayleigh scattering is positioned toward the direction normal to the laser sheet, whereas the ICCD camera for PLIF is shifted with a viewing angle of 6° as shown in Fig. 4.

3. Flame thickness analysis from experiments

Before proceeding to a direct comparison of experimental and numerical results, experiments are used to gather information concerning reactive scalar gradients for the different conditions under study; see Table 1. For low and moderate Reynolds numbers, the influence of velocity RMS u' and equivalence ratio Φ on the local flame thickness are known to be nonnegligible [23,24]. Indeed, even if the flame front can be still considered locally as a laminar flame wrinkled by the turbulent flow field, i.e., turbulent eddies are not able to broaden the preheat zone of the flame front, modifications of the local flame thickness can be a consequence of the flow-induced flame stretch. In the particular case of turbulent stratified flames, local variations of the equivalence ratio lead to changes in the flame surface area due to variations of the local propagation speed. The magnitude of the changes depends on the spatial distribution of fuel heterogeneities as well as the laminar flame propagation properties. The resulting increase of the flame surface leads to an additional flame stretch that must be also considered. Clearly, this effect must be taken into account in the analysis of the flame structure. Here, we deal first with the evaluation of the fuel heterogeneities effects on the local flame thickness. The local flame thermal thickness can be obtained from Rayleigh scattering images according to the definition

$$\delta_L = \frac{T_i - T_0}{|\nabla T|_{\max}},$$

where T_0 is the temperature of the fresh gas and T_i is the intermediate value corresponding to the maximum of the temperature gradient. The knowledge of $|\nabla T|_{\max}$ requires 3D information, which can be provided by a dual-plane Rayleigh scattering technique, as described by Soïka et al. [25]. From a single 2D Rayleigh scattering image, it is only possible to detect the projection of the temperature gradient onto the measurement plane. Such a procedure can lead to over estimation of the averaged laminar flame thickness $\langle \delta_L \rangle$ by an amount of 10 to 15%, as reported by De Goey [26]. However, this difficulty can be overcome by performing relative comparisons between the flame thickness obtained under various operating conditions rather than estimating absolute values of the flame thickness. Then the local flame thickness can be extracted from temperature images, along lines normal to the isotherm 500 K. In a first step of the analysis, results concerning homogeneous flames are now considered.

3.1. Flames stabilized in homogeneous mixtures

The first part of the analysis concerns the flow field and fuel parameters that may influence the flame inner structure. Typically, both velocity fluctuations and equivalence ratio can be considered through a turbulent Karlovitz number defined as $\mathrm{Ka_T} = (u'/S_L^0)^{3/2} \cdot (\delta_L^0/L_T)^{1/2}$. Various experimental published results are already available for different flame configurations such as (i) Bunsen flames, Buschmann et al. [27], Mansour et al. [28], Halter [29], (ii) V-shaped flames, Soïka et al. [25], and (iii) swirled flames, O'Young and Bilger [30]. These experiments have led to a series of databases in a wide range of values of the Karlovitz number, i.e., from 0.05 to 25. However, conclusions drawn by the authors of these previous works indicate different and sometimes opposite trends concerning the correlation between the mean normalized turbulent flame thickness and the turbulent Karlovitz number. The influence of this Karlovitz number can be studied by varying either the mixture or the turbulence characteristics.

The influence of the equivalence ratio has already been well identified and all the measurements indicate that, keeping constant the turbulent flow properties, an increase of equivalence ratio always produces an increase of the mean normalized flame thickness, at least for lean mixtures normalized flame thickness [26,31]. A compilation of results presented by Dinkelacker [31] clearly shows that for a bluff body and low swirl flames, a significant thinning of the thermal flame thickness is found for lean flames whereas for rich conditions the thermal thickness increases in turbulent flames (for $\mathrm{Ka} > 1$). A similar trend can be observed in our experimental results for two turbulence intensities (grids B and E), even if our absolute values of normalized flame thickness are significantly higher than the previous ones, see Fig. 5. Different reasons can explain these differences: As the first point, the geometrical configuration is different and the turbulence level used in the present work is quite low ($\mathrm{Re_T} \approx 100$). These flames are clearly

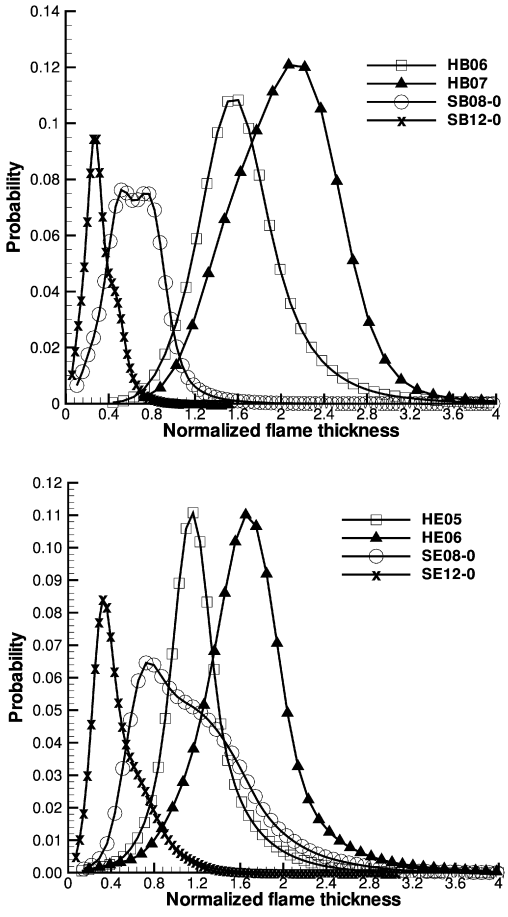

Fig. 5. PDF of the local flame thickness normalized by the laminar flame thickness $\delta_L^0(\langle\Phi\rangle)$ for the turbulence grids B (top) and E (bottom).

belonging to the flamelet regime (at least for homogeneous conditions). For low values of the Karlovitz number, experimental data available in the literature [25,31] show that the normalized flame thickness can be larger than unity (see Fig. 6). Next, the estimation of the maximum gradient along temperature profiles is very sensitive to noise and larger values of measured flame thickness can be reached. Moreover, only 2D measurements are reported in the present work, and the absolute value of the local flame thickness is over-estimated with respect to 3D measurements available, for instance, in Ref. [31].

We now focus the analysis on the mechanism that produces a modification of the local flame thickness during the interaction between the flame front and the turbulent flow field. The main effect of the turbulence induced fluctuations on the flame thickness is the flame stretch produced by small and large scales eddies [23,26]. This local stretch can be decomposed into two distinct parts: nonuniformity of the flow along the flame surface (tangential strain rate) and the flame curvature.

Influence of the local curvature on the flame thickness is now investigated. Dispersion of the results is limited by creating 20 regularly spaced bins for flame curvature analysis and computing the averaged values of the thermal flame thickness for the corresponding bins. For all the homogeneous cases a strong correlation between flame thickness and flame curvature is observed; see Fig. 7. Large positive flame curvatures are associated with large values of the local flame thickness and this result has been already observed by various authors for different flow configurations, in particular for Bunsen flames [29] and freely propagating flames [32]. The qualitative analysis of flame temperature images clearly points out this behavior; see

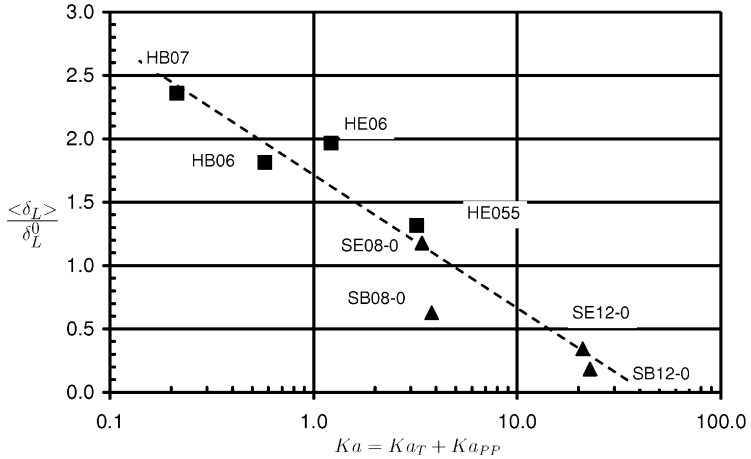

Fig. 6. Measured turbulent flame thickness normalized with the laminar unstretched flame thickness obtained using the Cantera software, for both homogeneous and stratified conditions, as a function of the Karlovitz number $\mathrm{Ka} = \mathrm{Ka_T} + \mathrm{Ka_{PP}}$. The dashed line corresponds to a power law fit of the data.

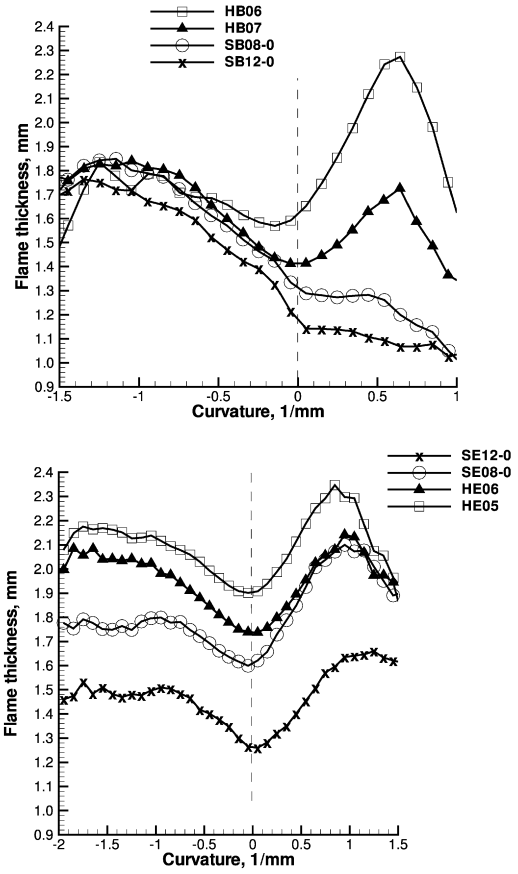

Fig. 7. Mean local flame thickness versus flame curvature for 20 regularly spaced bins for the different operating conditions: grid B (top) and grid E (bottom).

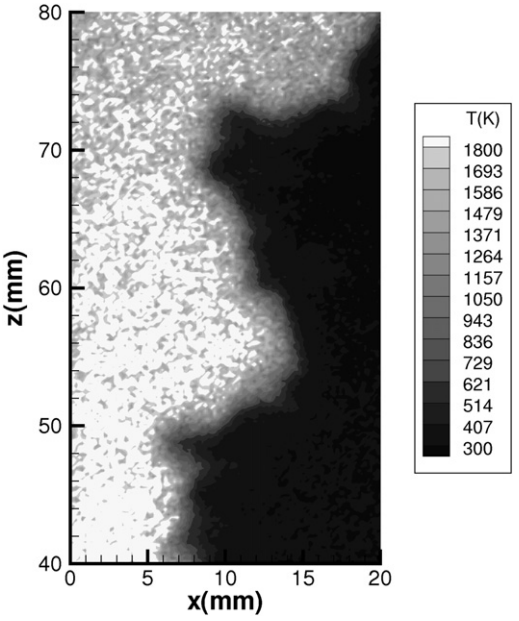

Fig. 8. Selected temperature field for the condition SE10-0.

Fig. 8. For negative curvatures, a similar correlation can be noticed and has been also reported by Chen and Bilger [24] for low turbulent Karlovitz number, i.e., $\mathrm{Ka_T} = 0.86$. This correlation explains also the increase of flame thickness RMS with the turbulence level (from $\langle \delta_L^{RMS} \rangle = 0.37$ mm for $u'/U = 3.7\%$ to $\langle \delta_L^{RMS} \rangle = 0.47$ mm for $u'/U = 7.5\%$ for an equivalence ratio $\Phi = 0.6$), since the flame curvature RMS is directly related to turbulence intensity [33].

In addition to the mechanisms just discussed, the effect of the strain rate on the flame thickness is more difficult to evaluate, since the measurement of this former quantity requires the projection of the velocity field along the tangent to the flame front. The numerical simulation of such a mechanism has been studied by Najm and Wyckoff [34], who investigated the interaction between a counterrotating vortex pair and a flame. Their results have evidenced a strong correlation between the flame thermal thickness and the strain rate. Indeed, tangential strain rate is expected to decrease (increase) the flame thickness when it is positive (negative).

3.2. Flames stabilized in stratified mixtures

We now turn our attention to the case of turbulent flames stabilized in stratified mixtures. In addition to the parameters encountered for homogeneous flames, the influence of spatial and temporal fluctuations of fuel concentration on local flame thickness must be evaluated. The study of the joint PDF of flame thickness and mixture fraction provides information on the role of the local mixture fraction in flame thickening or thinning, as shown by Fig. 9. For homogeneous conditions the joint PDF exhibits a globally circular shape and a nonzero RMS of the methane mole fraction. Indeed, these fluctuations of the methane mole fraction along the 500-K isotherm are due to the variations of strain rate and curvature that modify the burning rate locally. Now, for stratified flames, the joint PDF is found to be more asymmetrical and two zones can be clearly identified. The positive tail of the PDF (high values of flame thickness and low values of the fuel mole fraction) corresponds to locations far downstream the stabilizing rod where mean and fluctuating fuel concentrations are very low. The second zone is associated with a large range of fuel mole fraction giving the same local flame thickness, but rather smaller than for homogeneous flames, i.e., without equivalence ratio fluctuations. To illustrate this behavior, the mean normalized flame thickness can be compared for (i) homogeneous mixtures and (ii) stratified mix-

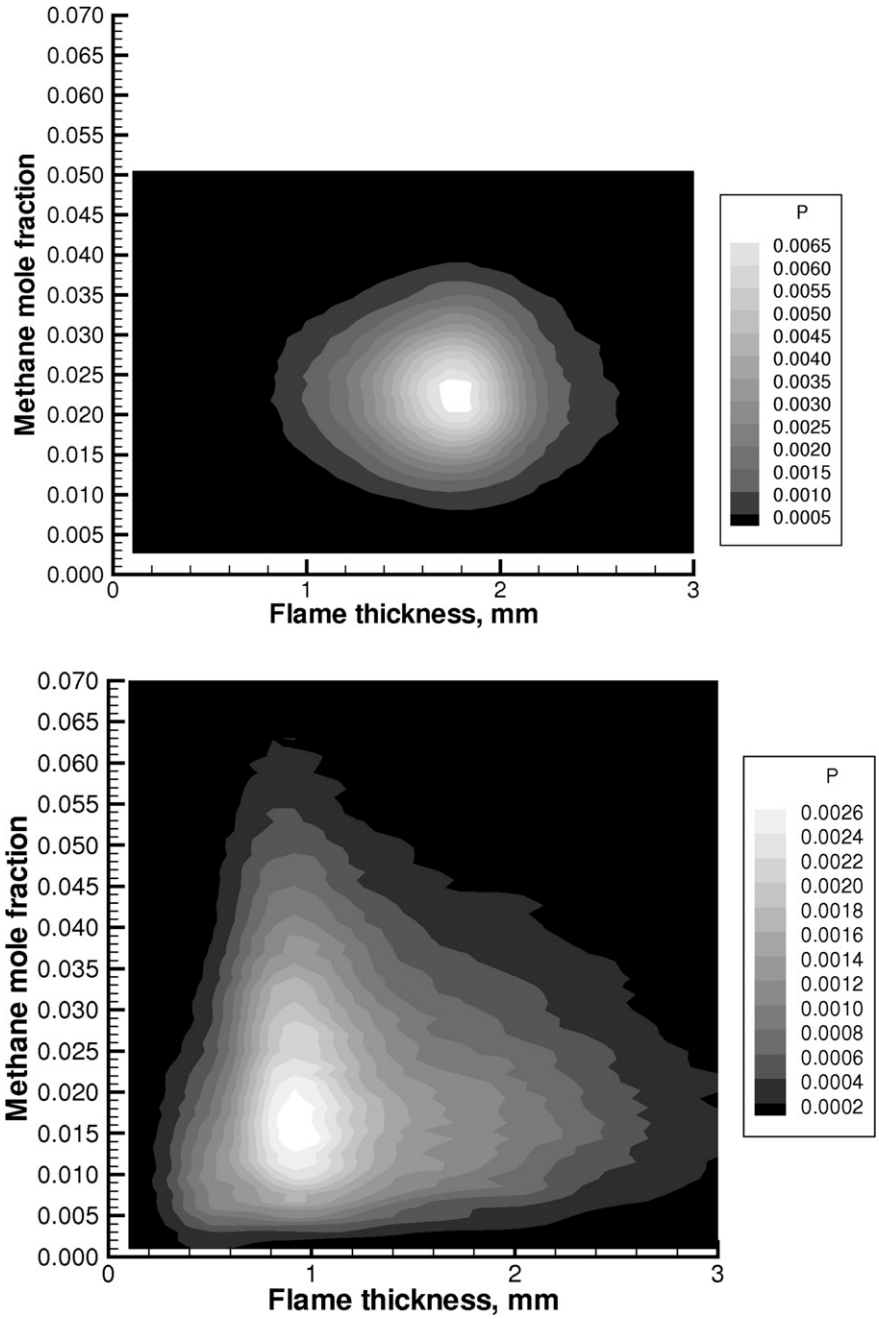

Fig. 9. Joint PDF of the local flame thickness normalized by the laminar flame thickness $\delta_L^0(\langle\Phi\rangle)$ and the mole fraction of methane at the isotherm 500 K, for homogeneous condition HE06 and stratified conditions SE12-0.

tures, for a given value of the mean equivalence ratio. This mean value is obtained by averaging the local equivalence ratio along the flame front as given by the location of the isoline of temperature 293 K; see Table 1. The mean normalized flame thickness $\langle\delta_L\rangle/\delta_L^0$ is found to be equal to 1.315 for the HE05 case and 1.178 for the SE08-0 case. This corresponds to a decrease of 10% for the stratified condition with respect to the homogeneous case. Thus the average laminar flame thickness is found to be lower for stratified conditions than for homogeneous conditions,

$$\frac{\langle\delta_L\rangle_S}{\delta_L^0(\langle\Phi\rangle)} < \frac{\langle\delta_L\rangle_H}{\delta_L^0(\Phi)},$$

Table 3
Experimental conditions and relevant parameters for the investigated homogeneous and stratified conditions

Name	$\langle\Phi\rangle$	Φ'	L_Φ (mm)	$S_L^0(\langle\Phi\rangle)$ (m/s)	$\delta_F(\langle\Phi\rangle)$ (mm)	$\delta_L^0(\langle\Phi\rangle)$ (mm)
HB06	0.60	–	–	0.111	0.93	0.62
HB07	0.69	–	–	0.189	0.62	0.40
HE05	0.53	–	–	0.068	1.51	1.06
HE06	0.6	–	–	0.111	0.93	0.62
SB08-0	0.49	0.15	2.7	0.051	2.15	1.56
SB12-0	0.37	0.16	3.2	0.020	6.74	5.28
SE08-0	0.54	0.14	3.5	0.071	1.45	1.01
SE12-0	0.42	0.20	4.9	0.029	4.20	3.20

Name	u'/S_L^0	L_T/δ_F	ΔS_L^0	Ka_T	Ka_{PP}	$Ka = Ka_T + Ka_{PP}$
HB06	1.25	5.9	–	0.58	0	0.58
HB07	0.74	8.8	–	0.21	0	0.21
HE05	3.46	4.0	–	3.21	0	3.21
HE06	2.14	6.6	–	1.22	0	1.22
SB08-0	2.75	2.55	0.060	2.85	0.9	3.80
SB12-0	6.98	0.82	0.022	20.42	2.3	22.73
SE08-0	3.34	4.20	0.073	2.98	0.4	3.40
SE12-0	8.22	1.45	0.048	19.54	1.4	20.97

Name	$\langle\delta_L\rangle$	$\langle\delta_L^{RMS}\rangle$	$\langle\delta_L\rangle/\delta_L^0$	$\langle\delta_L^{RMS}\rangle/\delta_L^0$
HB06	1.68	0.37	1.814	0.400
HB07	1.47	0.31	2.361	0.498
HE05	1.99	0.52	1.315	0.344
HE06	1.82	0.47	1.965	0.508
SB08-0	1.35	0.51	0.627	0.237
SB12-0	1.23	0.54	0.183	0.080
SE08-0	1.71	0.70	1.178	0.482
SE12-0	1.44	0.70	0.343	0.167

Notes. The laminar flame speed S_L^0 and thickness $\delta_L^0 = (T_i - T_0)/|\nabla T|_{max}$ are obtained from Cantera software, using a detailed GRI3.0 mechanism with a detailed transport description. The turbulent Karlovitz number is defined as $Ka_T = (u'/S_L^0)^{3/2} \cdot (\delta_L^0/L_T)^{1/2}$ according to the definition given by Peters [48]. δ_F is calculated through $\delta_F = (T_b - T_0)/|\nabla T|_{max}$, with T_b the temperature of the fully burned products.

where indices S and H stand respectively for stratified and homogeneous conditions.

The modification of the flame structure in terms of flame wrinkling or flame thickness is not only produced by the local flame stretch, i.e., by hydrodynamic straining together with flame propagation, but also by the variations of the flame propagation speed with mixture composition. In this way, the partial premixing or the small-scale fuel heterogeneities induce an additional stretch that can be expressed following Poinsot et al. [6] by

$$K_{PP} = \frac{\Delta w}{L_\xi},$$

where Δw is the amplitude of the variation of the flame propagation speed w measured at the flame location and L_ξ is the integral scalar length scale. In fact, the measurement of the flame propagation speed is a quite difficult task and Δw has been approximated by $\Delta S_L^0 = (S_L^0(\langle\Phi\rangle + \Phi'/2) - S_L^0(\langle\Phi\rangle - \Phi'/2))$, where Φ' is the equivalence ratio fluctuation. This approximation can lead to a small overestimation of Δw.

Thus, the additional stretch can be expressed using the following nondimensional number to take partial premixing into account:

$$Ka_{PP} = \frac{\Delta S_L^0}{L_\xi} \frac{\delta_L^0(\langle\Phi\rangle)}{S_L^0(\langle\Phi\rangle)}.$$

Typical values of Ka_{PP} for the operating conditions are reported in Table 3. It is worth noting that the corresponding values are not negligible, especially for lean conditions; see for instance the case SB08-0. The corresponding evolution of the normalized flame thickness for stratified conditions as a function of the total Karlovitz number $Ka = Ka_T + Ka_{PP}$ is reported in Fig. 7. From this analysis of the local flame structure subjected to stretch induced by turbulence or/and composition heterogeneities, we can conclude that there is a significant thinning effect that can be

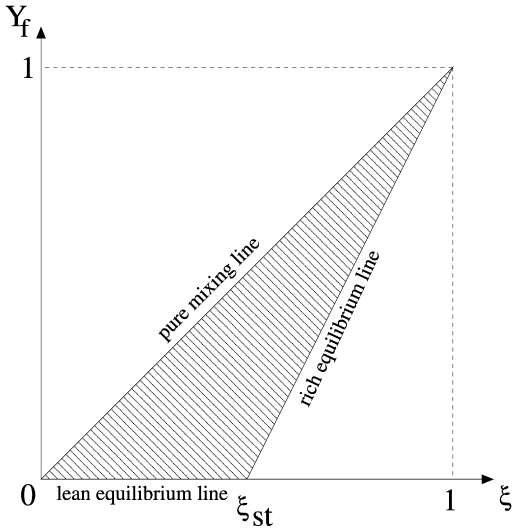

Fig. 10. Domain of definition $\mathcal{D}$ for the joint scalar PDF $\tilde{P}(\xi, Y_f)$ in the composition space.

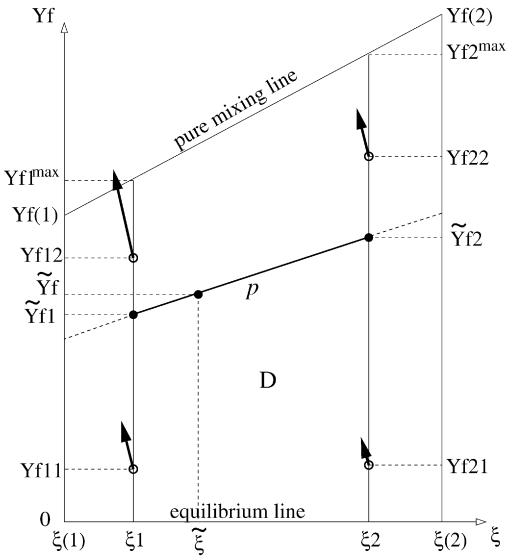

Fig. 11. Locations of the four delta functions in the domain $\mathcal{D}$.

associated with the Karlovitz number in both cases of homogeneous and stratified conditions.

The modeling and numerical simulation of such stratified flows is presented in the next section.

4. Description of the model

The modeling of stratified or more generally speaking partially premixed turbulent flames, such as the one described in the previous section, requires the use of at least two independent scalar variables, one for the progress of chemical reactions and a mixture fraction. Here we use the LW-P model of partially premixed combustion described by Robin et al. [17] and based on the simplified thermochemistry introduced by Libby and Williams [15]. In this thermochemistry, as long as the flow can be considered isenthalpic, all species mass fractions and temperature are related to the two characteristic scalars, namely the fuel mass fraction Y_f and the mixture fraction ξ.

In the present work, the mixture fraction is defined as $\xi = (Y_{N_2}^{\max} - Y_{N_2})/(Y_{N_2}^{\max} - Y_{N_2}^{\min})$, where Y_{N_2} is the mass fraction of nitrogen and the superscripts max and min correspond to pure air and fuel, respectively. The extreme situation where the mixture fraction ξ varies in the whole range, i.e., $0 \leqslant \xi \leqslant 1$, would correspond to a nonpremixed flame. As shown by Fig. 10, the domain $\mathcal{D}$ of the plane (ξ, Y_f) where these two variables are defined is bounded by three different straight lines, the pure mixing line $Y_f = \xi$, and the equilibrium lines for lean and rich mixtures $Y_f = 0$ and $Y_f = (\xi - \xi_{st})/(1 - \xi_{st})$, respectively. It is worth noticing that, in the present situation, by considering methane–air combustion the definition of mixture fraction becomes $\xi = 1 - Y_{N_2}/Y_{N_2}^{\max}$ with $Y_{N_2}^{\max} = Y_{N_2}^{\text{air}}$, the mass fraction of nitrogen in air.

4.1. Expression of the mean chemical reaction rate

As described by Robin et al. [17], a mass-weighted joint PDF of ξ and Y_f made of four Dirac delta functions is introduced:

$$\tilde{P}(\xi, Y_f) = \alpha \tilde{P}_1(Y_f)\delta(\xi - \xi_1) + (1-\alpha)\tilde{P}_2(Y_f)\delta(\xi - \xi_2). \quad (7)$$

$\tilde{P}_1$ and $\tilde{P}_2$ are the two conditional PDF at $\xi = \xi_1$ and $\xi = \xi_2$, defined as

$$\tilde{P}_1 = \beta\delta(Y_f - Y_{f11}) + (1-\beta)\delta(Y_f - Y_{f12}),$$
$$\tilde{P}_2 = \gamma\delta(Y_f - Y_{f21}) + (1-\gamma)\delta(Y_f - Y_{f22}), \quad (8)$$

where α, β, γ, ξ_1, ξ_2, Y_{fii} are the nine PDF parameters depending on the position in the flow field, as described by Fig. 11.

It has been shown [17] that, in the proposed LW-P model, the corresponding PDF shape relies eventually only on the first and second moments of Y_f and ξ. The knowledge of this PDF allows the evaluation of the mean chemical rate $\overline{\omega}$ that appears on the RHS of the transport equation for the mean value of the fuel mass fraction. This equation can be written as

$$\frac{\partial}{\partial t}(\overline{\rho}\tilde{Y}_f) + \frac{\partial}{\partial x_k}(\overline{\rho}\tilde{u}_k\tilde{Y}_f) = \frac{\partial}{\partial x_k}\left(\overline{\rho D\frac{\partial Y_f}{\partial x_k}} - \overline{\rho u_k'' Y_f''}\right) + \overline{\omega} \quad (9)$$

with

$$\overline{\omega} = \overline{\rho} \iint_{\mathcal{D}} \frac{\omega(\xi, Y_f)}{\rho(\xi, Y_f)} \tilde{P}(\xi, Y_f)\, d\xi\, dY_f, \tag{10}$$

where $\mathcal{D}$ is the domain of definition of the PDF in the composition space.

In Eq. (10) the instantaneous rate of fuel consumption ω is written by assuming a single-step global chemistry,

$$\omega = \rho(\xi, Y_f) B(\xi) \big(Y_f - Y_f^{\min}\big) \exp\big(-T_a / T(\xi, Y_f)\big), \tag{11}$$

where T_a is the activation temperature, B the pre-exponential factor, and $Y_f^{\min}$ the minimum value of Y_f, $Y_f^{\min} = 0$ for lean mixtures and $Y_f^{\min} = (\xi - \xi_{st})/(1 - \xi_{st})$ for rich mixtures. The activation temperature has been considered as constant and the pre-exponential factor is assumed to be a function of the mixture fraction ξ. Calculations are performed using the PREMIX module of the Chemkin II library [35] to determine the pre-exponential factor and the activation temperature values as follows: the pre-exponential factor is selected so that the laminar burning velocity obtained with a detailed kinetic scheme is recovered. The GRI-2.11 detailed mechanism of Bowman et al. [36] is used for this purpose. The activation temperature is selected so that the slope of the chemical production rate $d\omega/dY_f$ on the burned side is recovered. This yields $T_a = 25{,}000$ K. The rates of fuel consumption $\omega = f(Y_f)$ for various values of the equivalence ratio and obtained with (i) the detailed kinetic scheme and (ii) the single step global reaction given by Eq. (11) are reported in Fig. 12. From this figure, the following conclusions can be drawn: (i) For lean mixtures, the rates of fuel consumption obtained by using the single-step global reaction scheme are in very good agreement with those obtained from the detailed chemical scheme. (ii) For rich mixtures, fuel is still available, whereas no more dioxygen is present and the fuel mass fraction is not representative of the combustion process across the flame. Obviously, fuel mass fraction cannot be used as a progress variable for such rich mixtures.

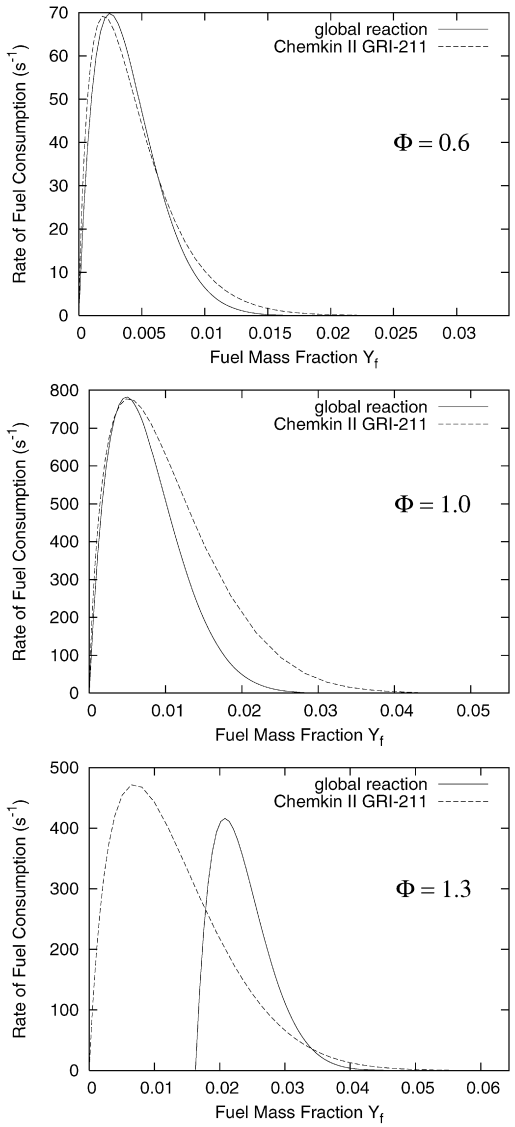

Fig. 12. Rate of fuel consumption $\omega/\rho = f(Y_f)$ with $\Phi = 0.6$, $\Phi = 1.0$, and $\Phi = 1.3$.

4.2. Balance equations

Following the description of the model presented in the previous section, five balance equations, i.e., those for the first- and second-order scalar quantities, are needed to provide a closed system, allowing inter alia the calculation of the mean chemical rate:

- Mean mixture fraction:

$$\frac{\partial}{\partial t}(\overline{\rho}\tilde{\xi}) + \frac{\partial}{\partial x_k}(\overline{\rho}\tilde{u}_k\tilde{\xi}) = \frac{\partial}{\partial x_k}\left(\overline{\rho D \frac{\partial \xi}{\partial x_k}} - \overline{\rho u_k'' \xi''}\right). \tag{12}$$

- Variance of the mixture fraction:

$$\frac{\partial}{\partial t}(\overline{\rho \xi''^2}) + \frac{\partial}{\partial x_k}(\tilde{u}_k \overline{\rho \xi''^2}) = \frac{\partial}{\partial x_k}\left(\overline{\rho D \frac{\partial \xi''^2}{\partial x_k}} - \overline{\rho u_k'' \xi''^2}\right) - 2\overline{\rho D \frac{\partial \xi''}{\partial x_k}\frac{\partial \xi''}{\partial x_k}} - 2\overline{\rho u_k'' \xi''}\frac{\partial \tilde{\xi}}{\partial x_k}. \tag{13}$$

- Mean fuel mass fraction:

$$\frac{\partial}{\partial t}(\overline{\rho}\tilde{Y}_{\mathrm{f}}) + \frac{\partial}{\partial x_k}(\overline{\rho}\tilde{u}_k\tilde{Y}_{\mathrm{f}}) = \frac{\partial}{\partial x_k}\left(\overline{\rho D\frac{\partial Y_{\mathrm{f}}}{\partial x_k}} - \overline{\rho u_k'' Y_{\mathrm{f}}''}\right) + \overline{\omega}. \tag{14}$$

- Variance of the fuel mass fraction:

$$\frac{\partial}{\partial t}\left(\overline{\rho Y_{\mathrm{f}}''^2}\right) + \frac{\partial}{\partial x_k}\left(\tilde{u}_k\overline{\rho Y_{\mathrm{f}}''^2}\right) = \frac{\partial}{\partial x_k}\left(\overline{\rho D\frac{\partial Y_{\mathrm{f}}''^2}{\partial x_k}} - \overline{\rho u_k'' Y_{\mathrm{f}}''^2}\right) - 2\overline{\rho D\frac{\partial Y_{\mathrm{f}}''}{\partial x_k}\frac{\partial Y_{\mathrm{f}}''}{\partial x_k}} - 2\overline{\rho u_k'' Y_{\mathrm{f}}''}\frac{\partial \tilde{Y}_{\mathrm{f}}}{\partial x_k} + 2\overline{Y_{\mathrm{f}}''\omega}. \tag{15}$$

- Cross correlation:

$$\frac{\partial}{\partial t}(\overline{\rho Y_{\mathrm{f}}''\xi''}) + \frac{\partial}{\partial x_k}(\tilde{u}_k\overline{\rho Y_{\mathrm{f}}''\xi''}) = \frac{\partial}{\partial x_k}\left(\overline{\rho D\frac{\partial Y_{\mathrm{f}}''\xi''}{\partial x_k}} - \overline{\rho u_k'' Y_{\mathrm{f}}''\xi''}\right) - 2\overline{\rho D\frac{\partial Y_{\mathrm{f}}''}{\partial x_k}\frac{\partial \xi''}{\partial x_k}} - \overline{\rho u_k'' Y_{\mathrm{f}}''}\frac{\partial \tilde{\xi}}{\partial x_k} - \overline{\rho u_k'' \xi''}\frac{\partial \tilde{Y}_{\mathrm{f}}}{\partial x_k} + \overline{\xi''\omega}. \tag{16}$$

In these equations, turbulent scalar fluxes are modeled by using a simple gradient law approximation

$$\overline{\rho u_k'' \xi''} = -\overline{\rho} D_{\mathrm{T}}\frac{\partial \tilde{\xi}}{\partial x_k}; \qquad \overline{\rho u_k'' Y_{\mathrm{f}}''} = -\overline{\rho} D_{\mathrm{T}}\frac{\partial \tilde{Y}_{\mathrm{f}}}{\partial x_k}$$

$$\overline{\rho u_k'' \xi''^2} = -\overline{\rho} D_{\mathrm{T}}\frac{\partial \widetilde{\xi''^2}}{\partial x_k};$$

$$\overline{\rho u_k'' Y_{\mathrm{f}}''^2} = -\overline{\rho} D_{\mathrm{T}}\frac{\partial \widetilde{Y_{\mathrm{f}}''^2}}{\partial x_k} \quad \text{and}$$

$$\overline{\rho u_k'' Y_{\mathrm{f}}'' \xi''} = -\overline{\rho} D_{\mathrm{T}}\frac{\partial \widetilde{Y_{\mathrm{f}}''\xi''}}{\partial x_k}, \tag{17}$$

where $D_{\mathrm{T}} = C_\mu k^2/(\mathrm{Sc}_{\mathrm{T}}\epsilon)$ with $C_\mu = 0.09$ is used. k and ϵ are respectively the turbulent kinetic energy and its dissipation, and Sc_{T} is a turbulent Schmidt number set to its usual value of 0.7.

It must be noticed here that such a model cannot predict flame-generated turbulence that may be associated to countergradient diffusion. A full second-order model that will contain such a mechanism and will be applicable to partially premixed conditions is currently under development [37]. We now turn our attention to the important problem raised by the closure of the mean scalar dissipation terms.

4.3. Scalar dissipation terms

Concerning the passive scalar ξ, the mean dissipation term is closed using a linear relaxation model for the fluctuation decay rate:

$$\overline{\rho\epsilon_\xi} = \overline{\rho D\frac{\partial \xi''}{\partial x_k}\frac{\partial \xi''}{\partial x_k}} = \frac{\overline{\rho\xi''^2}}{\tau_\xi} \approx \frac{\overline{\rho\xi''^2}}{R_\xi \tau_{\mathrm{T}}}. \tag{18}$$

More attention must now be paid to the closure of the mean scalar dissipation of the reactive species.

Indeed, the experimental analysis reported in the previous section of this paper shows that equivalence ratio fluctuations do not increase the local flame thickness. In fact, experiments have revealed that, under the conditions under study, partial premixing can even lead to a small thinning of the local flame thickness. This information means clearly that the use of a closure expression as Eq. (18) for the reactive scalar, as done in another previous study [38], is far from being suitable, since reactive scalar gradients are fixed by chemical reaction (i.e., by the flame thickness $1/\delta_{\mathrm{L}}$) rather than by turbulence. This previous discussion emphasizes that mean reactive scalar dissipation terms require further attention. It is well known that the closure of the dissipation functions that are present in Eqs. (15) and (16) is one of the most critical points in turbulent combustion modeling, since these functions, together with chemical reaction, drive the evolution of the PDF shape in the composition space. As shown by Anand and Pope [39] and discussed recently by Mura et al. [10], the closure of the dissipation of the reactive scalar, Y_{f} in the present work, requires special care in the specific case of premixed combustion. In the limiting regime where the reactive flow is made of local infinitely thin flamelets, Libby and Bray [40] have established an expression that relates the mean scalar dissipation directly to the mean chemical rate. Using the reactive scalar Y_{f}, the corresponding relationship is

$$-2\overline{\rho\epsilon_{Y_{\mathrm{f}}}} = \overline{\omega}\left(Y_{\mathrm{f}}^{\max} - 2\tilde{Y}_{\mathrm{f}} + Y_{\mathrm{f}}^{\min}\right) - 2\,\overline{\omega Y_{\mathrm{f}}''}. \tag{19}$$

Since this pioneering work, Borghi and co-workers [41,42] and Swaminathan and Bray [43] have proposed modeled transport equations for the mean reactive scalar dissipation in the case of fully premixed reactive flows.

Concerning the reactive variable, we have here to deal with the two mean scalar dissipation terms $\overline{\rho\epsilon_{Y_{\mathrm{f}}}}$ and $\overline{\rho\epsilon_{\xi Y_{\mathrm{f}}}}$ appearing in Eqs. (15) and (16) and defined as

$$\overline{\rho\epsilon_{Y_{\mathrm{f}}}} = \overline{\rho D\frac{\partial Y_{\mathrm{f}}''}{\partial x_k}\frac{\partial Y_{\mathrm{f}}''}{\partial x_k}}, \qquad \overline{\rho\epsilon_{Y_{\mathrm{f}}\xi}} = \overline{\rho D\frac{\partial Y_{\mathrm{f}}''}{\partial x_k}\frac{\partial \xi''}{\partial x_k}}. \tag{20}$$

To close these two terms we propose to use an algebraic model based on the recent developments made

by Mura et al. [44]. In fact, the closure presented below is a rigorous generalization of our earlier derivation.

In the absence of combustion, i.e., when $\omega \approx 0$, or when the thickened flames regime of turbulent combustion [45] is reached ($\tau_{\text{chem}} \ll \tau_{\text{T}}$), Eqs. (13), (15), and (16) for the second-order scalar quantities reduce to a single one, and in this specific case, a linear relaxation model for the fluctuation decay rate can be used for Y_{f},

$$\overline{\rho\epsilon_{Y_{\text{f}}}}_{\text{NR}} = \frac{\overline{\rho Y_{\text{f}}''^2}}{\tau_{Y_{\text{f}}}} \approx \frac{\overline{\rho Y_{\text{f}}''^2}}{R_{Y_{\text{f}}}\tau_{\text{T}}},$$
$$\overline{\rho\epsilon_{Y_{\text{f}}\xi}}_{\text{NR}} = \frac{\overline{\rho Y_{\text{f}}''\xi''}}{\tau_{Y_{\text{f}}\xi}} \approx \frac{\overline{\rho Y_{\text{f}}''\xi''}}{R_{Y_{\text{f}}\xi}\tau_{\text{T}}}, \tag{21}$$

where the subscript NR stands for nonreactive conditions.

At the other limit, when the flamelet regime is reached, i.e., for $\tau_{\text{chem}} \gg \tau_{\text{T}}$, it can be shown that, under the assumption of large Reynolds numbers, the three mean dissipation terms are not independent quantities but are linked together by the following important relationship, see Mura et al. [44]:

$$\begin{aligned}2(1+\tilde{A})\overline{\rho\epsilon_{Y_{\text{f}}\xi}}_{\text{R}} - 2\tilde{A}\overline{\rho\epsilon_{\xi}} - 2\overline{\rho\epsilon_{Y_{\text{f}}}}_{\text{R}} \\ = \overline{\omega}\big(\tilde{Y}_{\text{f}}^{\max} - 2\tilde{Y}_{\text{f}} + \tilde{Y}_{\text{f}}^{\min}\big) \\ + (1+\tilde{A})\overline{\omega\xi''} - 2\overline{\omega Y_{\text{f}}''}.\end{aligned} \tag{22}$$

In Eq. (22), $\tilde{A}$ is the mean slope of the equilibrium line, defined so that $A = 0$ and $A = 1/(1-\xi_{\text{st}})$ for lean and rich mixtures, respectively. $Y_{\text{f}}^{\max}$ and $Y_{\text{f}}^{\min}$ are defined by the composition space; thus $\tilde{Y}_{\text{f}}^{\max} = \tilde{\xi}$ and $\tilde{Y}_{\text{f}}^{\min} = \tilde{A}(\tilde{\xi} - \xi_{\text{st}})$.

It must be pointed out that fluctuations around the equilibrium line slope have been neglected in Eq. (22), namely $A'' \approx 0$.

Taking into account Eq. (22), we now propose to use the following closures for the reactive contributions to the two mean dissipation terms,

$$\begin{aligned}-2\overline{\rho\epsilon_{Y_{\text{f}}}}_{\text{R}} \\ = (\tilde{Y}_{\text{f}_{\max}} - 2\tilde{Y} + \tilde{Y}_{\text{f}_{\min}})\overline{\omega} - 2\overline{Y_{\text{f}}''\omega} \\ + \frac{(1+\tilde{A})(1-\tilde{A})}{\tilde{Y}_{\text{f}_{\max}} - \tilde{Y}_{\text{f}_{\min}}}\widetilde{\xi''^2}\overline{\omega} \\ + (1+\tilde{A})\big(\theta + (1-\theta)\tilde{A}\big) \\ \times \left(-2\overline{\rho\epsilon_{\xi}} - 2\overline{\rho u_k''\xi''}\frac{\partial\tilde{\xi}}{\partial x_k}\right) \\ - (1+\tilde{A})\left(-\overline{\rho u_k''Y_{\text{f}}''}\frac{\partial\tilde{\xi}}{\partial x_k} - \overline{\rho u_k''\xi''}\frac{\partial\tilde{Y}_{\text{f}}}{\partial x_k}\right) \\ + \tilde{A}(-2\overline{\rho\epsilon_{\xi}}),\end{aligned} \tag{23}$$

$$\begin{aligned}-2\overline{\rho\epsilon_{Y_{\text{f}}\xi}}_{\text{R}} \\ = -\overline{\xi''\omega} + \frac{(1-\tilde{A})}{\tilde{Y}_{\text{f}_{\max}} - \tilde{Y}_{\text{f}_{\min}}}\widetilde{\xi''^2}\overline{\omega} \\ + \big(\theta + (1-\theta)\tilde{A}\big)\left(-2\overline{\rho\epsilon_{\xi}} - 2\overline{\rho u_k''\xi''}\frac{\partial\tilde{\xi}}{\partial x_k}\right) \\ + \overline{\rho u_k''Y_{\text{f}}''}\frac{\partial\tilde{\xi}}{\partial x_k} + \overline{\rho u_k''\xi''}\frac{\partial\tilde{Y}_{\text{f}}}{\partial x_k},\end{aligned} \tag{24}$$

with θ and $(1-\theta)$ given by

$$\theta = \frac{\tilde{Y}_{\text{f}} - \tilde{Y}_{\text{f}}^{\min}}{\tilde{Y}_{\text{f}}^{\max} - \tilde{Y}_{\text{f}}^{\min}}, \qquad (1-\theta) = \frac{\tilde{Y}_{\text{f}}^{\max} - \tilde{Y}_{\text{f}}}{\tilde{Y}_{\text{f}}^{\max} - \tilde{Y}_{\text{f}}^{\min}}.$$

It must be emphasized here that expressions (23) and (24) have the expected limiting behaviors in particular the one anticipated for the regime of infinitely thin flamelet and fully premixed combustion. Expressions (23) and (24) are more general than those we have previously proposed in our recent work on scalar dissipation in partially premixed flames [44]. They are obtained by considering the limiting behaviors of Eqs. (15) and (16) in the flamelet regime of turbulent combustion. In this situation, reactive scalar variance and cross scalar fluctuation levels can be obtained through the following algebraic relationships:

$$\begin{aligned}\big(\overline{\rho Y_{\text{f}}''^2}\big)^{\max} &= \overline{\rho}\big(\tilde{Y}_{\text{f}}^{\max} - \tilde{Y}_{\text{f}}\big)\big(\tilde{Y}_{\text{f}} - \tilde{Y}_{\text{f}}^{\min}\big) \\ &\quad + \big(\theta + (1-\theta)\tilde{A}^2\big)\overline{\rho\xi''^2}, \\ \overline{\rho Y_{\text{f}}''\xi''} &= \big(\theta + (1-\theta)\tilde{A}\big)\overline{\rho\xi''^2}.\end{aligned}$$

Finally, in the present work, the turbulent scalar flux that appears in Eqs. (23) and (24) is closed by using the standard turbulent diffusivity approximation as given by Eq. (17).

A straightforward strategy to recover the two limits, namely the thickened flame regime given by Eq. (21) and the flamelet regime given by Eqs. (23) and (24), is now to use a linear bridging function depending on the available segregation rate level S. This strategy leads to

$$-2\overline{\rho\epsilon_{Y_{\text{f}}}} = -(1-S).\frac{\overline{\rho Y_{\text{f}}''^2}}{R_{Y_{\text{f}}}\tau_{\text{T}}} - 2S\overline{\rho\epsilon_{Y_{\text{f}}}}_{\text{R}}, \tag{25}$$

$$-2\overline{\rho\epsilon_{Y_{\text{f}}\xi}} = -(1-S).\frac{\overline{\rho Y_{\text{f}}''\xi''}}{R_{Y_{\text{f}}\xi}\tau_{\text{T}}} - 2S\overline{\rho\epsilon_{Y_{\text{f}}\xi}}_{\text{R}} \tag{26}$$

with $R_{\xi} = R_{Y_{\text{f}}} = R_{Y_{\text{f}}\xi}$.

In Eqs. (25) and (26), the set of Eq. (21) is recovered for $S = 0$ and conversely Eqs. (23) and (24) are recovered for $S = 1$. The following expression for S is proposed

$$S = \frac{\overline{\rho Y_{\text{f}}''^2} - (\overline{\rho Y_{\text{f}}''^2})^{\min}}{(\overline{\rho Y_{\text{f}}''^2})^{\max} - (\overline{\rho Y_{\text{f}}''^2})^{\min}}, \tag{27}$$

where $(\overline{\rho Y_f''^2})^{\min}$ is the minimum possible value for the variance, i.e., mixing in the absence of chemistry, and $(\overline{\rho Y_f''^2})^{\max}$ is the maximum value [44]. The latter has been defined above and $(\overline{\rho Y_f''^2})^{\min}$ is related to the nonreactive mixing-induced fluctuations of the reactive scalar and it is simply given by

$$\left(\overline{\rho Y_f''^2}\right)^{\min} = \left(\lambda + (1-\lambda)\tilde{A}^2\right)\overline{\rho\xi''^2}.$$

4.4. Numerical conditions

The LW-P model described in the previous sections has been implemented in the computational fluid dynamics (CFD) code developed by EDF, *Code_Saturne*; see Archambeau et al. [46]. *Code_Saturne* is a parallel general-purpose three-dimensional low-Mach-number CFD code based on a finite volume method. The set of equations considered consists of the averaged Navier–Stokes equations for incompressible flows completed with equations for turbulence modeling and for additional scalars (enthalpy, concentration of species, and possibly user-defined scalars). The time marching scheme is based on a prediction of the velocity field followed by a pressure correction step. Equations for turbulence and scalars are resolved separately afterward. The discretization in space is based on the fully conservative, unstructured finite-volume framework, with a fully colocated arrangement for all variables.

The numerical CFD code makes it possible to perform LES simulations, but in the present calculations, turbulent mixing is represented through a conventional one-point two-equation k–ϵ model. Experimental results for the nonreactive flow field are used to specify boundary conditions in order to reproduce grid turbulence decay correctly. An unstructured grid of approximately 21,000 cells has been generated to represent half of the physical domain. The corresponding mesh is depicted in Fig. 13. The top side (respectively bottom side) of the domain is approximated by an outlet boundary condition (respectively an inlet boundary condition). Boundary conditions on the left side of the computational domain are given by the symmetry of the flow. On the right side, wall conditions are imposed for $z < 0$, i.e., along the convergent exit of the channel. For $z > 0$, the boundary condition on the right side is approximated by a special condition, which can be either an inlet or an outlet. From a numerical point of view, combustion is stabilized by the recirculation zone produced downstream of a nonheated half-rod of diameter 1 mm.

Inlet boundary conditions must be specified with special care, since they may have a strong influence on the development of combustion inside the computational domain. Nevertheless, this task is complicated by several constraints: (i) first, measurements

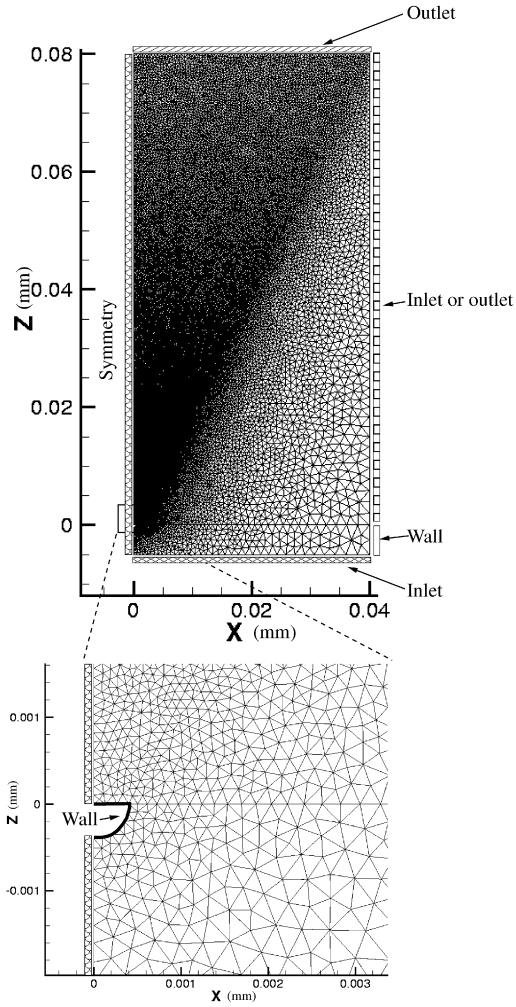

Fig. 13. Unstructured grid used for numerical simulation.

of all variables at the exact location of the numerical inlet boundary are not always available; (ii) moreover, an additional constraint results from the difficulty of measuring some of the various transported variables on which the turbulent combustion model relies. This is especially true for the turbulence mean dissipation rate ϵ. As a consequence, to specify inlet boundary conditions as realistically as possible for the velocity field, we have first compared numerical and experimental results in the simpler case of a nonreactive mixture in homogeneous decaying grid turbulence. This preliminary task has been repeated for each condition and then studied in reactive situations corresponding to cases HE06, SE10-0, SB08-0, and SB12-0. In this process, mean velocity and mean turbulent kinetic energy are directly taken from experimental data, whereas the turbulence dissipation rate ϵ is chosen in such a manner that the experimental grid turbulence decay is recovered; see Fig. 14. In each

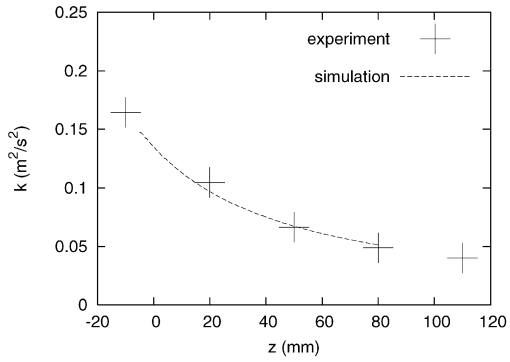

Fig. 14. Grid E turbulence decay. The mean dissipation at the inlet has been adjusted to recover the experimental trend.

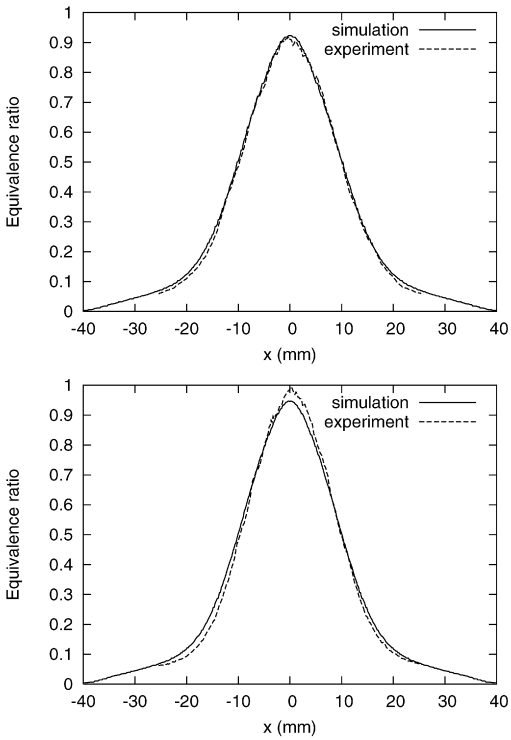

Fig. 15. Equivalence ratio profiles at $z = 42.5$ and 70 mm, case SE10-0.

case, the corresponding inlet conditions for the velocity field are $\tilde{u} = 3.2$ m/s, $\tilde{v} = 0$ m/s. Concerning the turbulence fields, the inlet boundary conditions for the turbulence kinetic energy and its dissipation rate are different for grids B and E. The turbulence kinetic energy levels are specified from the ADL measurements which are available at the location of computational inlet boundaries, $k = 0.15\ \mathrm{m}^2/\mathrm{s}^2$ for grid E and $k = 0.058\ \mathrm{m}^2/\mathrm{s}^2$ for grid B, whereas the turbulence mean dissipation rate ϵ has been chosen in such a manner that the grid turbulence decay is recovered: $\epsilon = 10\ \mathrm{m}^2/\mathrm{s}^3$ for grid E and $\epsilon = 2.3\ \mathrm{m}^2/\mathrm{s}^3$ for grid B. The resulting numerical grid turbulence decay for grid E has been reported in Fig. 14. Finally, concerning the inlet boundary conditions for scalars, the profiles of the mean and variance of the scalars ξ and Y_f at the inlet are directly obtained from measurements: $\tilde{Y}_\mathrm{f} = \tilde{\xi}$ and $\widetilde{Y''^2_\mathrm{f}} = \widetilde{\xi''^2} = \widetilde{Y''_\mathrm{f}\xi''}$. Resulting profiles of equivalence ratio mean and variance are presented in Figs. 15 and 16 at two different distances downstream of the stabilizing rod for a nonreactive flow field.

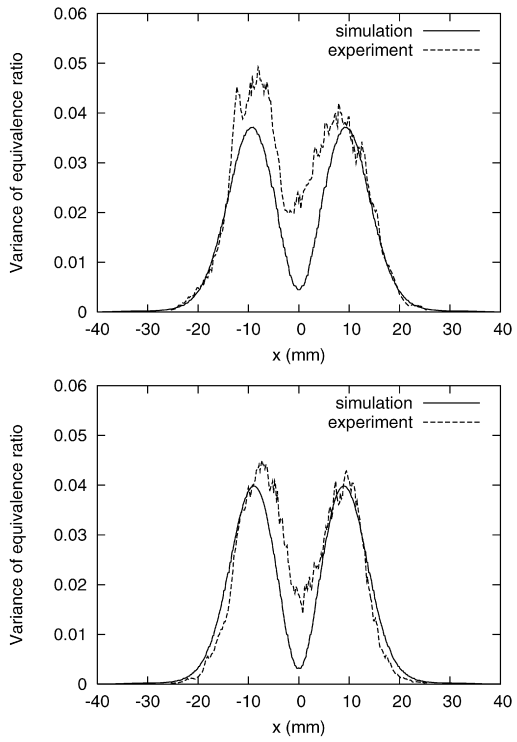

Fig. 16. Variance of equivalence ratio at $z = 42.5$ and 70 mm, case SE10-0.

5. Numerical simulation of the reactive flows

The numerical part of the work has been coordinated with the previously described experimental study to evaluate the influence of fuel–air heterogeneities on turbulent V-shaped flames. As pointed out before, the analysis of the physical phenomena involved in stratified combustion indicates clearly the need for simultaneous knowledge of the local progress variable and composition, this latter quantity being provided by the mixture fraction. Moreover, as emphasized in the previous section, the cross-dissipation rate $\overline{\rho\epsilon_{\xi Y}}$ plays an important role in the modeling. Therefore, the models that we develop

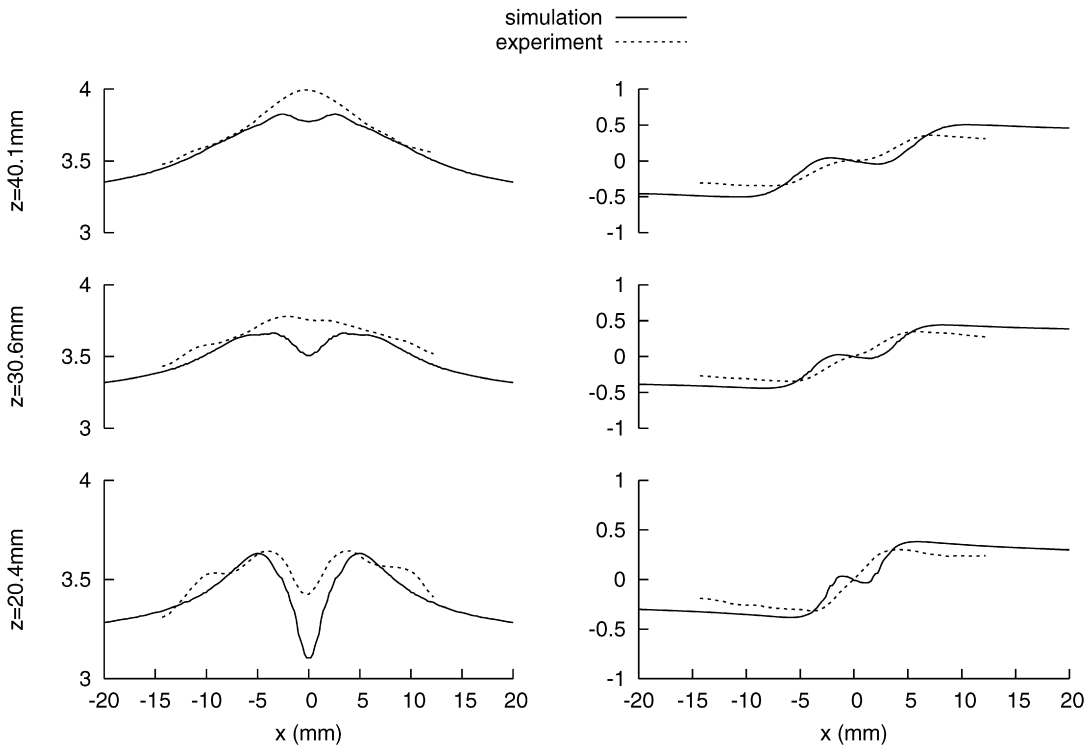

Fig. 17. Mean longitudinal and transverse velocity profiles in m s^{-1} at three distinct locations, $z = 20.4$, 30.6, and 40.1 mm, for homogeneous conditions, case HE06.

need to be validated against experimental data with sufficient accuracy. In the present study, comparisons between experimental and numerical data are performed for different homogeneous and stratified conditions, as reported in Table 1. The case of homogeneous mixtures has been studied first, in order to obtain reference cases and allow further direct comparisons with stratified situations. In a first step, the predictivity of the model is evaluated by comparing numerical results with experimental data. In particular, mean and fluctuating velocity, temperature and progress variable fields are considered. In a second step, numerical simulations are used to compare the results obtained with different stratification conditions with an emphasis on correlations for which measurements are not available, such as the mean reaction rate $\overline{\omega}$ and the cross scalar correlation $\overline{\rho Y_{\mathrm{f}}'' \xi''}$, since such quantities are expected to be strongly influenced by the fuel–air ratio heterogeneities of the incoming flow.

5.1. Numerical simulations versus experimental data

5.1.1. Fully premixed combustion

The first step of the comparison between experimental data and numerical results is carried out in the case of fully premixed turbulent flames. In this special simplified situation, since the mixture fraction is constant, the four-Dirac-delta-functions PDF given by Eq. (7) degenerates toward a two-Dirac-delta-functions PDF and the equations to be used are Eq. (14) for the mean fuel mass fraction and Eq. (15) for the variance of the fuel mass fraction. The main objective of this first comparison is to validate the model setup for the turbulent scalar flow, together with the chemistry representation, in terms of mean velocity and progress variable profiles.

The numerical solution for the velocity field is compared with experimental data at three different distances downstream of the stabilizing rod; see Fig. 17. Profiles are shown in Fig. 17 only where experimental data are available. Good agreement between numerical and experimental data is observed for the main properties of the reactive velocity fields, in particular, in terms of the flow acceleration along the centerline in the burned gases and the flame-generated outward deflection in the fresh gases. A difference can be observed for the longitudinal velocity profile in the vicinity of $x = 0$ mm, just behind the stabilizing rod. Experimental data exhibit a slight decrease at this location, which is not reproduced by the numerical simulation. This velocity decay is a consequence of the flow recirculation induced by the rod, and the modeling of this recirculation zone and the

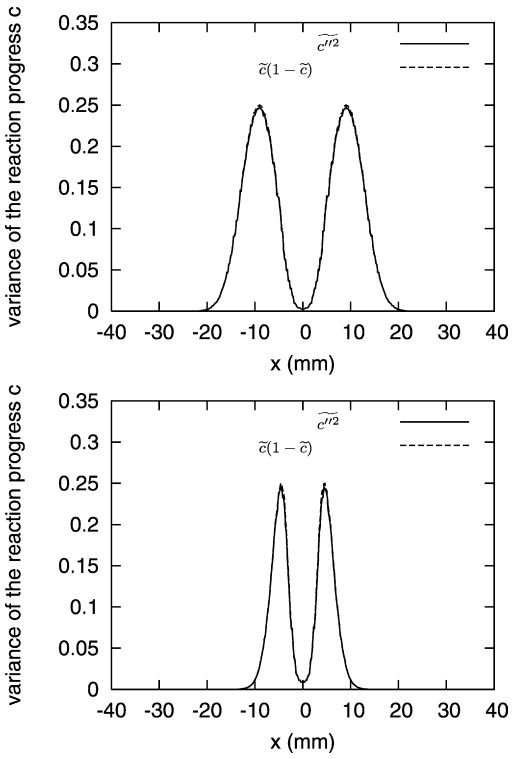

Fig. 18. Variance of the reaction progress profiles at $z = 42.5$ and 70 mm for homogeneous conditions, case HE06.

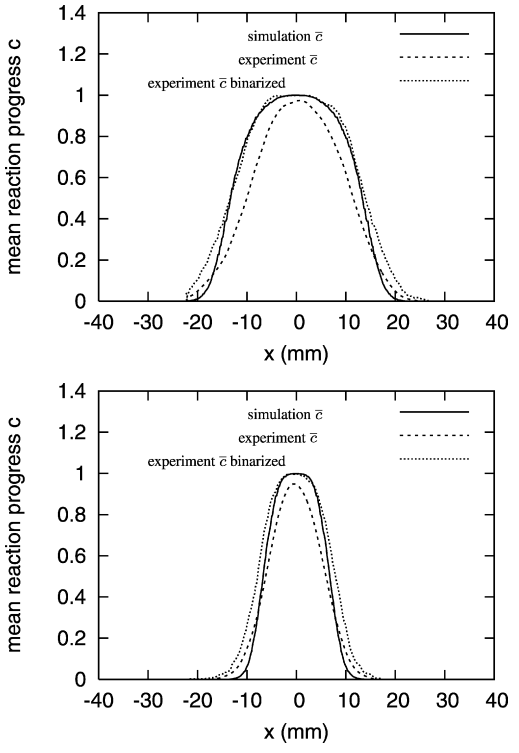

Fig. 19. Mean progress variable profiles at $z = 42.5$ and 70 mm for homogeneous conditions, case HE06.

weak acceleration induced by the expansion of the burned gases at this small value of the equivalence ratio can explain this overestimation. Similar differences have been obtained in the study carried out by Bell et al. [47], who investigated turbulent premixed V-shaped flame using both experiments and direct numerical simulations.

Experimental measurements provide the Reynolds mean temperature field $\overline{T}$ from which the Reynolds mean progress variable $\bar{c}$ can be obtained. Numerical simulation provide Favre mean temperature $\tilde{T}$ and Favre mean progress variable $\tilde{c}$. To evaluate Reynolds average values from Favre average values, the following expression has been used for any quantity q,

$$\bar{q} = \frac{\widetilde{T^* q}}{\widetilde{T^*}} = \frac{\int q T^*(\xi, Y_f)\tilde{P}(\xi, Y_f)\,d\xi\,dY_f}{\int T^*(\xi, Y_f)\tilde{P}(\xi, Y_f)\,d\xi\,dY_f}, \qquad (28)$$

where $T^*(\xi, Y_f) = T(\xi, Y_f)/W(\xi, Y_f)$, with T the temperature and W the molecular weight. This relation is strictly valid provided that pressure variations remain small enough.

Fig. 18 shows that $(1-\tilde{c})\tilde{c}$ and $\widetilde{c''^2}$ profiles are very similar, showing that with the proposed modeling approach, turbulent combustion is found to take place in the flamelet regime.

The experimental mean progress variable field can be obtained from two different processes, i.e., using binarized or nonbinarized tomographic images. Fig. 19 compares numerical results with experimental results when using these two different methodologies.

Whatever the type of experimental data processing used, Fig. 19 evidences very good agreement between numerical and experimental results. Nevertheless, as shown by the figure, the agreement is slightly better when the experimental method relying on binarized images is used.

5.1.2. *Partially premixed combustion*

The more general case of partially premixed turbulent combustion is now considered. The study is performed in the case of the stratified condition SE1.0-0 with an equivalence ratio varying from unity at the center of the wind tunnel to zero at the edge of the wind tunnel. Longitudinal and transversal velocity profiles presented in Fig. 20 show a very good agreement between numerical results and corresponding experimental data. It is worth noting that no velocity decrease downstream of the heated rod ($x = 0$) has been measured. Indeed, in stratified conditions, the heat release along the x-axis is not homogeneous, and the large values of the equivalence ratio in the vicinity of the rod lead to a flow acceleration stronger

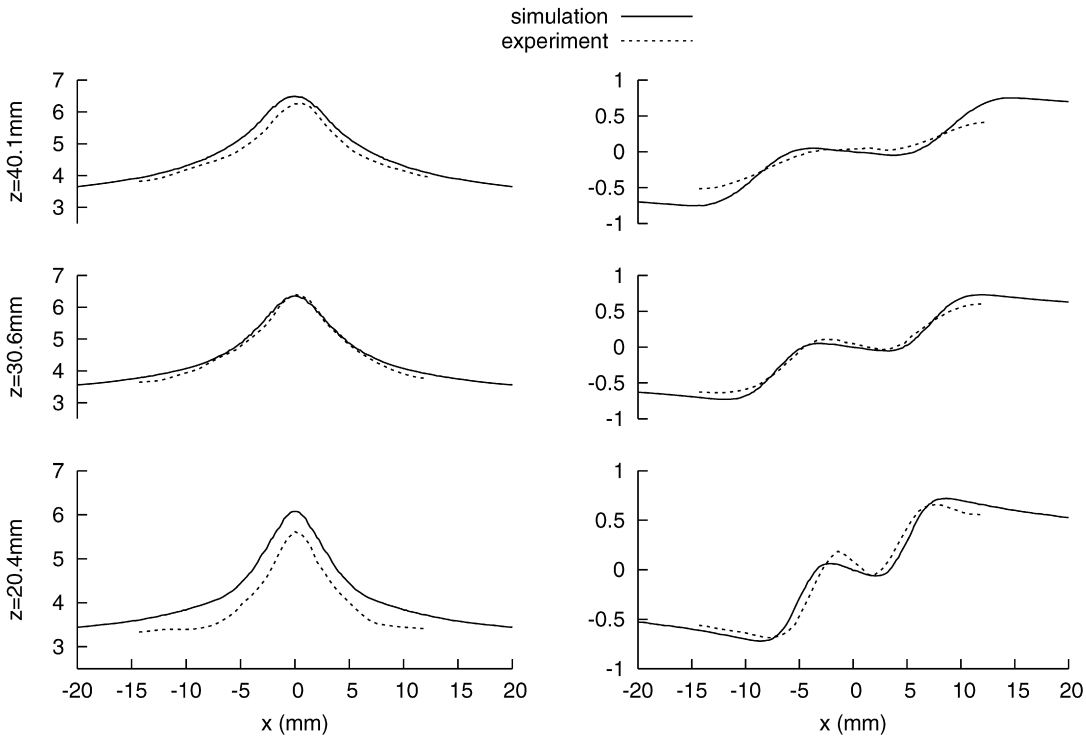

Fig. 20. Mean longitudinal and transverse velocity profiles in m s^{-1} at three distinct locations, $z = 20.4$, 30.6, and 40.1 mm, for stratified conditions SE10-0.

than the one observed on the lateral sides of the flow. Accordingly, there is no need for a detailed model to represent the flow recirculation at the rod location, since the flow field is mainly controlled by the strong heat release near $x = 0$ in this case.

Numerical and experimental profiles of the mean progress variable at two different distances from the rod location are presented in Fig. 21. The experimental one corresponds to binarized tomographic images. As displayed in this figure, the agreement between experimental data and numerical results is good, which shows the ability of the LW-P model presented in the previous section to deal with partially premixed combustion. In the following and last section, numerical results are used to highlight the flame response to fuel–air heterogeneities.

5.2. Analysis of stratified flames through the LW-P closure

As reported in the previous section, the LW-P model, as described previously, has been tested first against experiments for the conditions of turbulence obtained when using the grid E. Calculations carried out under both homogeneous (HE06) and stratified (SE1.0-0) conditions have shown a satisfactory agreement with experiments.

In a second step, we now present and discuss a series of numerical results obtained for flames stabilized under stratified lean ($\langle\Phi\rangle = 0.8$ to $\langle\Phi\rangle = 0$) or stratified rich ($\langle\Phi\rangle = 1.2$ to $\langle\Phi\rangle = 0$) conditions. In this second part of the analysis, the cases SB08-0 and SB1.2-0 of Table 1 have been retained for comparisons between experimental and numerical data. Numerical profiles of the mean progress variable obtained for those conditions are compared to experiments in Figs. 22 and 23. The results obtained for condition SB0.8-0 are in very good agreement with experiments whereas, at first sight, the agreement seems to be less satisfactory for conditions SB1.2-0. In fact, in the latter conditions, one can notice that the model predicts a good spatial development of the V-shaped flame since the differences observed between the experiment and the numerical simulation remains constant indicating that only the first stage of the flame growth in the vicinity of the flame holder has been overestimated. We explain this feature as follows: within the present approach, the burned gas composition is not limited by chemical equilibrium but by the global reaction. This approximation has no influence in fully lean conditions like these of SB0.8-0 because the differences between one step chemistry representation with only CO_2 and H_2O as combustion products and chemical equilibrium are very small

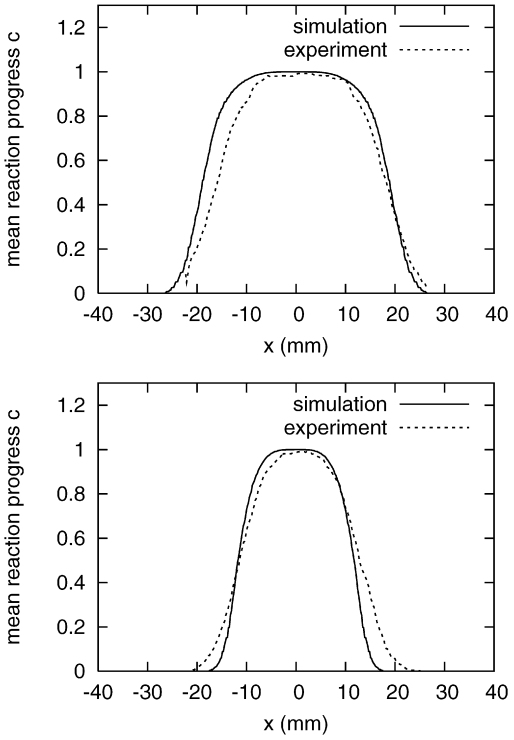

Fig. 21. Mean progress variable profiles (binarized tomographic images) at $z = 42.5$ and 70 mm for stratified conditions SE10-0.

in this case. In contrast, for fuel–air compositions around stoichiometry, as in the case SB1.2-0, we are now considering, the differences between the adiabatic temperature obtained from a detailed description of chemical species at equilibrium or from fully oxidized combustion products such as CO_2 and H_2O are expected to become more significant, leading to an overestimated heat release factor and, eventually, to an overestimated mean flame angle.

Mean and variance of the progress variable are considered in Figs. 24 and 25. The two V-shaped flames exhibit strongly different spatial developments downstream of the flame holder. This can be explained by considering these two figures, together with the mixture fraction field as given by Fig. 26. This latter figure clearly shows that

- In the vicinity of the flame holder, the mixture fraction field is first strongly deviated by flame expansion; the mean gradients of mixture fraction and progress variable tend to follow the same trend: therefore the flame propagates across the mixture fraction gradient.
- Downstream of the flame holder, at a distance of approximately $z = 0.015$ m, the flame brush finally crosses the mean stoichiometric isoline $\tilde{\xi} = \xi_{st}$ (see Figs. 24 and 25), leading to a strong deflection of the mean flame front.

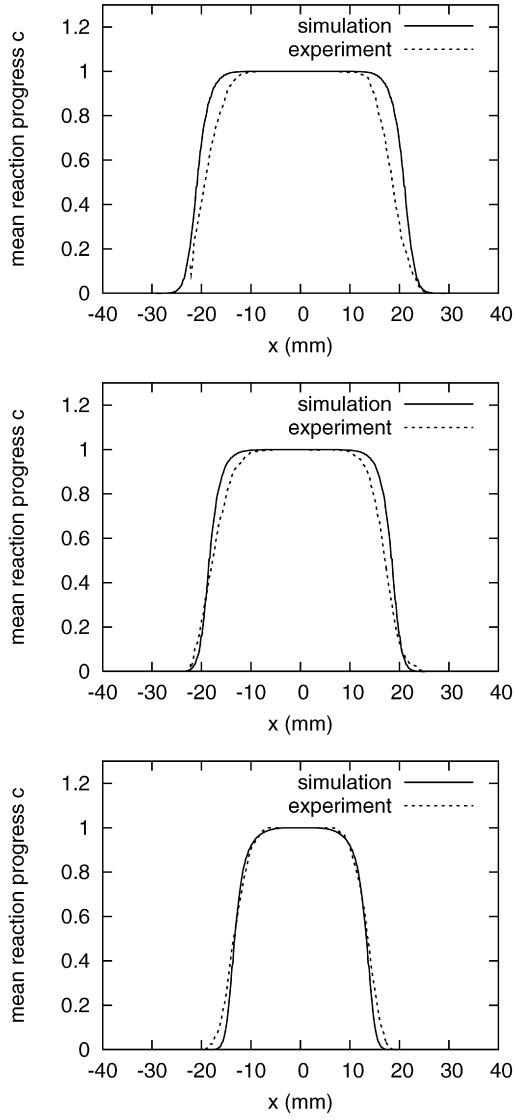

Fig. 22. Mean progress variable profiles at $z = 42.5$, 60, and 70 mm for stratified conditions SB08-0.

This behavior is also clearly visible on the mean reaction rate field given in Fig. 27 and on the fuel mass fraction field given in Fig. 28. One can also notice that, as expected, an excess of fuel remains along the centerline in the case SB1.2-0, as illustrated by Fig. 28.

Following our previous application of the LW-P model to lean partially premixed reactive flows [17], it is interesting to take a closer look at the behavior of the cross correlation between the fuel mass fraction and the mixture fraction variables; see Fig. 29. In

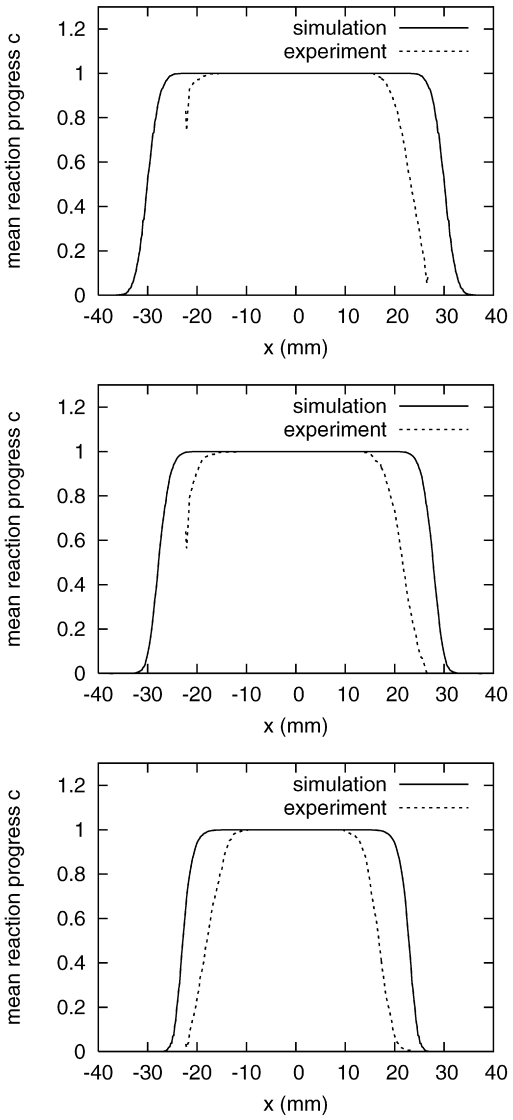

Fig. 23. Mean progress variable profiles at $z = 42.5$, 60, and 70 mm for stratified conditions SB12-0.

the LW-P model, this quantity is directly connected to the slope of the fluctuation line used to build the PDF shape; see Fig. 30.

The slope of this straight line is defined in Fig. 11 and is given by the following relationship:

$$p = \frac{\overline{\rho \xi'' Y_{\mathrm{f}}''}}{\overline{\rho \xi''^2}}.$$

Further details concerning its sign have been discussed in Ref. [17]. The corresponding field is depicted in Fig. 30.

Considering Figs. 29 and 30, the evolution of the slope p can be explained as follows. As the mixture fraction ξ increases from the left to the centerline, the value of p first decreases from unity to zero in the region of fuel-lean burned products. Indeed, since Y_{f} is zero for fully burned products and this whatever the value of ξ provided it corresponds to lean mixtures, this results in no fluctuations of Y_{f} behind the mean flame brush. As stoichiometric conditions are reached, fluctuations of fuel mass fraction become possible in the fully burned products resulting in a value of p that differs from zero. Finally, under conditions alongside the flame holder, the mixture is expected to be rich and fluctuations of Y_{f} can now occur in the burned products along the equilibrium trajectory, as given by $Y_{\mathrm{f_{min}}}(\xi) = (\xi - \xi_{\mathrm{st}})/(1 - \xi_{\mathrm{st}})$.

6. Conclusions

Partially premixed rod-stabilized methane–air turbulent stratified flames have been studied from experimental, modeling and numerical points of view. The experimental study, as well as its numerical counterpart, has been performed for different conditions of upstream stoichiometry and turbulence. Such flames are characterized by large-scale mean scalar gradients and important scalar fluctuations.

Simultaneous measurements by PLIF on acetone and two-dimensional Rayleigh scattering have been used to characterize the local flame structure (curvature, flame thickness, and fuel mole fraction at the fresh reactants side of the flame front), whereas the velocity field measurements have been performed by PIV. The direct comparisons of the results obtained by the two experimental and numerical approaches, based on the mean flow velocity and the Reynolds average mean progress variable, have shown very good agreement and, in particular, have demonstrated the ability of the LW-P model to deal with reactive flows with stratified conditions involving strong gradients of equivalence ratio. More precisely, the following conclusions can be drawn from experimental and numerical results concerning both situations of homogeneous and stratified upstream mixtures:

In the case of homogeneous flames, we have pointed out and characterized the strong interaction between flame stretch and flame thickness for a large range of values of the physical parameters that control the flame stretch (equivalence ratio and velocity variance) and the mechanisms (strain rate and flame curvature) which drive the flame stretch. In particular, we observe a very clear correlation between thermal flame thickness and flame curvature in all cases considered. For a flame thickness below a threshold value, the increase appears to be almost linear, for both negative and positive curvatures, with higher slopes for the positives curvatures. Indeed, an increase

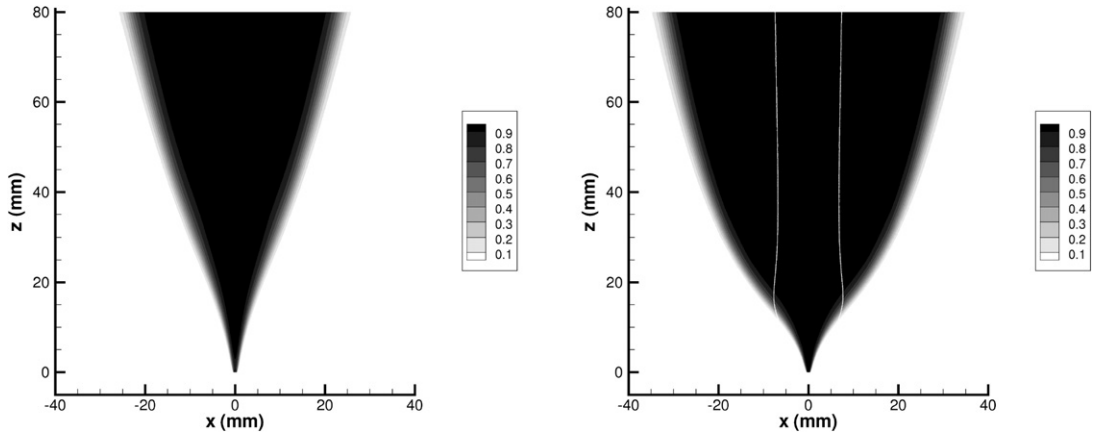

Fig. 24. Mean progress variable field for stratified conditions SB08-0 and SB12-0. Stoichiometric isoline $\tilde{\xi} = \xi_{st}$ is also depicted.

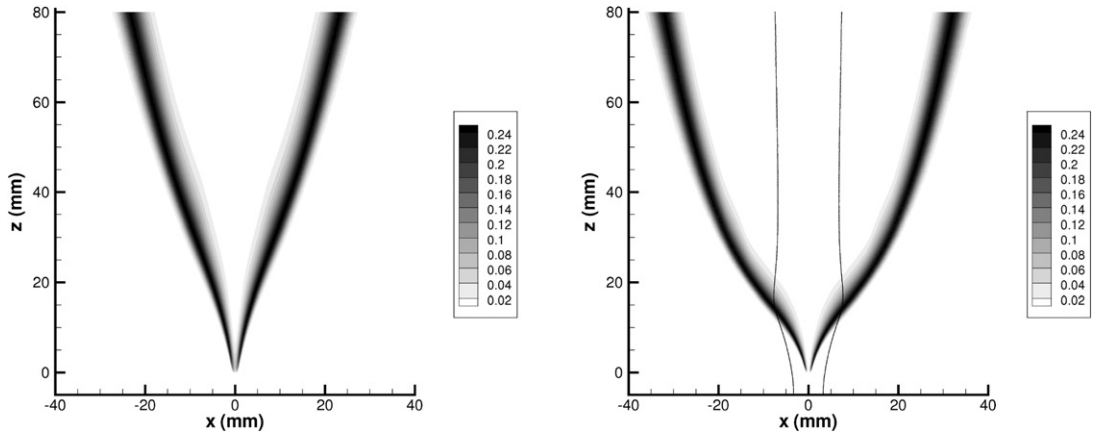

Fig. 25. Progress variable variance field for stratified conditions SB08-0 and SB12-0. Stoichiometric isoline $\tilde{\xi} = \xi_{st}$ is also depicted.

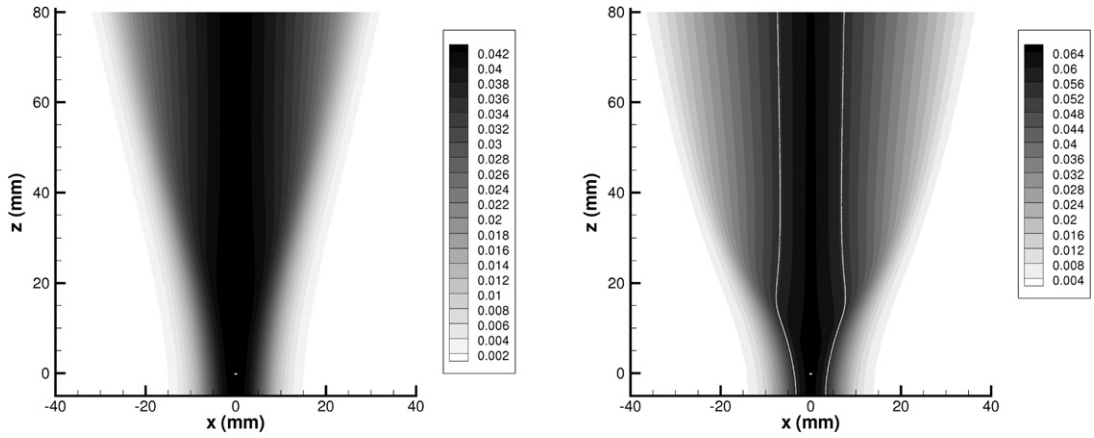

Fig. 26. Mixture fraction for stratified conditions SB08-0 and SB12-0. Stoichiometric isoline $\tilde{\xi} = \xi_{st}$ is also depicted.

of flame stretch leads to a decrease of the normalized flame thickness. From the experimental results, we conclude that the effect of turbulence on the local flame thickness should be interpreted in terms of local stretch components (strain rate and curvature) that can vary by an order of magnitude depend-

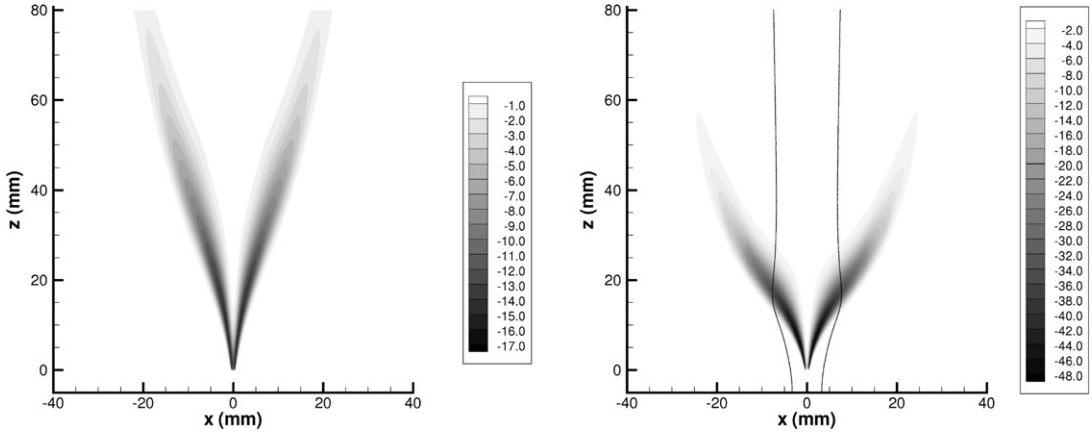

Fig. 27. Mean chemical rate $\overline{\omega}$ / $\overline{\rho}$ (s^{-1}) for stratified conditions SB08-0 and SB12-0. Stoichiometric isoline $\tilde{\xi} = \xi_{st}$ is also depicted.

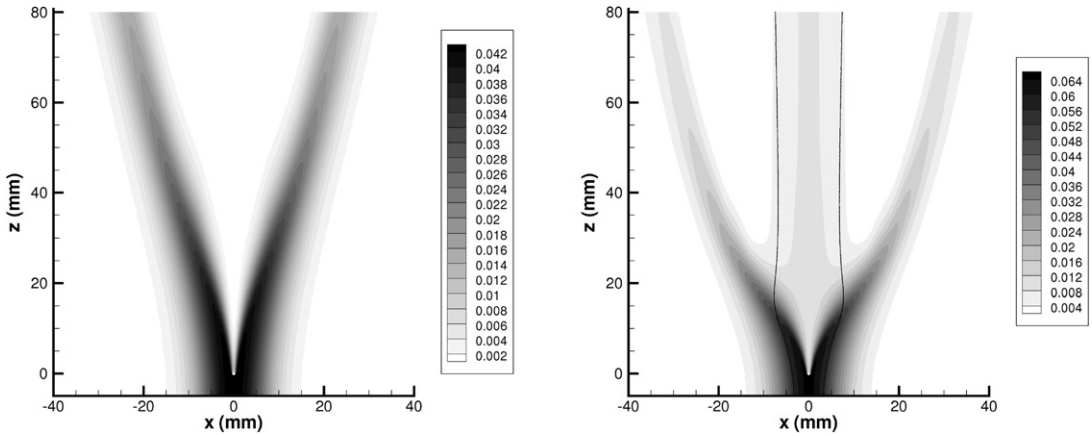

Fig. 28. Fuel mass fraction for stratified conditions SB08-0 and SB12-0. Stoichiometric isoline $\tilde{\xi} = \xi_{st}$ is also depicted.

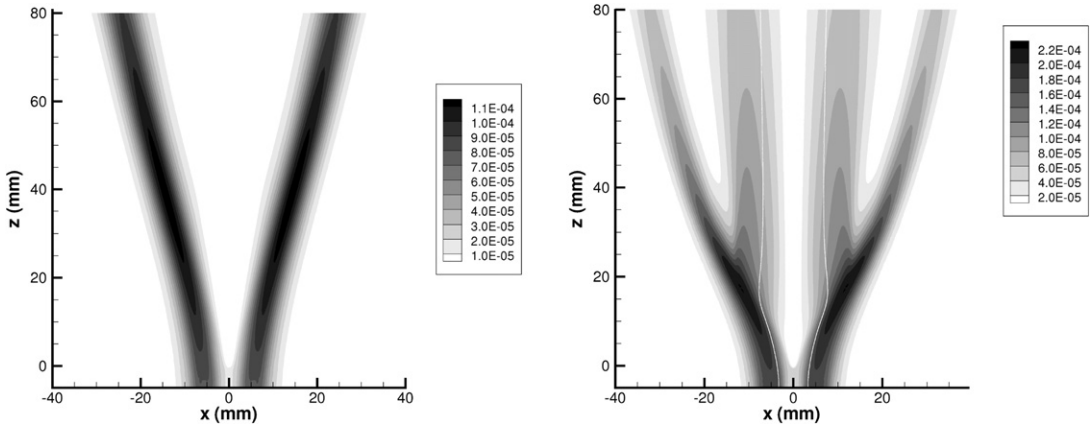

Fig. 29. Covariance $\widetilde{Y_f''\xi''}$ for stratified conditions SB08-0 and SB12-0. Stoichiometric isoline $\tilde{\xi} = \xi_{st}$ is also depicted.

ing on the flame configuration (Bunsen, stagnating, freely-propagating, etc.), rather as a global parameter.

For stratified flames, equivalence ratio fluctuations interact with the local flame fronts leading to an additional stretch which may be nonnegligible. This ad-

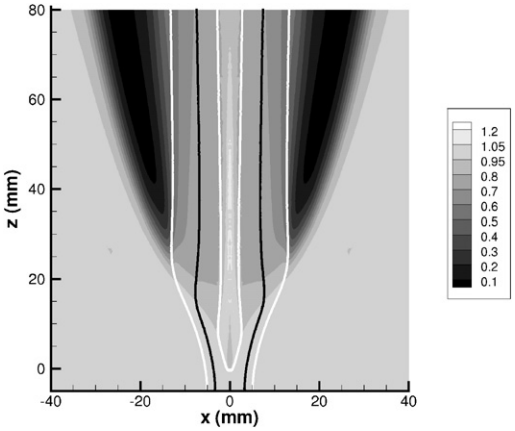

Fig. 30. Slope p of the fluctuation line as given by the ratio of the cross correlation between fuel mass fraction and mixture fraction and mixture fraction variance in case SB12-0. Stoichiometric isoline $\tilde{\xi} = \xi_{st}$ is also depicted (black line). Two isolines corresponding respectively to $\xi_1 = \xi_{st}$ and $\xi_2 = \xi_{st}$ are also represented (white lines).

ditional stretch leads also to a thinning of the normalized flame thickness. Indeed, for a same mean equivalence ratio measured along the flame front, a stratified flame is thinner than the corresponding homogeneous one.

The analysis of the numerical model and the successful comparisons made between experiments and numerical results have clearly shown that the LW-P model including a new closure for the scalar dissipation rates adapted to mixtures with variable stoichiometry is able to deal with strong stratification effects under both fuel-lean and fuel-rich conditions. Significant differences of behavior have been observed in these two situations. Finally, the study of fuel-rich conditions has led to an interesting investigation of joint reactive and nonreactive scalar dynamics.

From the modeling point of view, the representation of scalar small scales has been addressed and special care has been taken to close the scalar dissipation terms. Conversely, some efforts are still necessary to improve the turbulent mixing representation and a second-order model is currently under development to cope with this need. Such a model will allow to deal with flame-generated turbulence and countergradient diffusion effects in partially premixed conditions. Finally, the extension of the present model for the mean chemical rate, which relies currently on a skeletal description of the joint scalar PDF based on two or four Dirac delta functions, to consider detailed chemistry effects still remains a challenging task.

Acknowledgments

V. Robin, A. Mura, and M. Champion thank EDF and CNRS for their financial support. They are also indebted to C. Losier (LCD, ENSMA) for technical assistance.

References

[1] Y. Ra, C.K. Cheng, Proceedings of the Fifth Int. Symp. on Diagnostics and Modeling of Combustion in Internal Engines, Japan, 2001, pp. 251–257.
[2] T. Kang, D.C. Kyritsis, Proc. Combust. Inst. 31 (2007) 1075–1083.
[3] N. Pasquier, B. Lecordier, M. Trinité, A. Cessou, Proc. Combust. Inst. 31 (2007) 1567–1574.
[4] A. Pires-da-Cruz, A.M. Dean, J.M. Grenda, Proc. Combust. Inst. 28 (2000) 1925–1932.
[5] Y.M. Marzouk, A.F. Ghoniem, H.N. Najm, Proc. Combust. Inst. 28 (2000) 1859–1866.
[6] T. Poinsot, D. Veynante, A. Trouvé, G.R. Ruetch, Proceeding of the Summer Program, Center for Turbulence Research, Stanford, 1996, pp. 111–141.
[7] J. Zhou, K. Nishida, T. Yoshizaki, H. Hiroyasu, SAE Technical Paper number 982563.
[8] C. Jimenez, B. Cuenot, T. Poinsot, D.C. Haworth, Combust. Flame 128 (2002) 1–21.
[9] D. Garrido-Lopez, S. Sarkar, R. Sangras, Proc. Combust. Inst. 30 (2004) 621–628.
[10] A. Mura, F. Galzin, R. Borghi, Combust. Sci. Technol. 175 (7) (2003) 1–37.
[11] B. Renou, A. Boukhalfa, D. Puechberty, M. Trinité, Combust. Flame 123 (2000) 507–521.
[12] Y.S. Cho, D.A. Santavicca, SAE Technical Paper number 932715.
[13] J. Hélie, A. Trouvé, Proc. Combust. Inst. 27 (1998) 891–898.
[14] Y. Moriyoshi, H. Morikawa, T. Kamimoto, T. Hayashi, SAE Technical Paper number 962087.
[15] P.A. Libby, F.A. Williams, Combust. Sci. Technol. 161 (2000) 351–390.
[16] K.N.C. Bray, M. Champion, P.A. Libby, Combust. Sci. Technol. 174 (7) (2002) 167–174.
[17] V. Robin, A. Mura, M. Champion, P. Plion, Combust. Sci. Technol. 178 (10–11) (2006) 1843–1870.
[18] O. Degardin, B. Renou, A. Boukhalfa, Exp. Fluids 40 (2006) 452–463.
[19] B. Renou, E. Samson, A.M. Boukhalfa, Combust. Sci. Technol. 176 (2004) 1867–1890.
[20] F. Scarano, M.L. Reithmuller, Exp. Fluids Suppl. 29 (2000) S51–S60.
[21] M.C. Thurber, R.K. Hanson, Exp. Fluids 30 (2001) 93–101.
[22] D.A. Knaus, S.S. Satler, F.C. Gouldin, Combust. Flame 141 (2005) 253–270.
[23] C.J. Sung, J.B. Liu, C.K. Law, Combust. Flame 106 (1996) 168–183.
[24] Y.C. Chen, R. Bilger, Combust. Sci. Technol. 167 (2001) 187–222.

[25] A. Soïka, F. Dinckelaker, A. Leipertz, Proc. Combust. Inst. 27 (1998) 785–792.
[26] P. de Goey, Proc. Combust. Inst. 30 (2005) 859–866.
[27] A. Buschmann, F. Dinckelaker, F. Scheffer, M. Scheffer, J. Wolfrum, Proc. Combust. Inst. 26 (1996) 437–445.
[28] M.S. Mansour, N. Peters, Y.C. Chen, Proc. Combust. Inst. 27 (1998) 767–773.
[29] F. Halter, PhD thesis, Universite d'Orléans, France, 2005.
[30] F. O'Young, R.W. Bilger, Combust. Flame 109 (1997) 682–700.
[31] F. Dinckelacker, Proceedings of the First European Symposium on Combustion, ECM2003 Orléans, France, 2003.
[32] D. Thévenin, Proc. Combust. Inst. 30 (2005) 629–637.
[33] B. Renou, PhD thesis, University of Rouen, France, 1999.
[34] H.N. Najm, P.S. Wyckoff, Combust. Flame 110 (1997) 92–112.
[35] R.J. Kee, F.M. Rupley, J.A. Miller, SANDIA Report SAN89-8009 UC-401, 1989.
[36] C.T. Bowman, R.K. Hanson, W.C. Gardiner, V. Lissianski, M. Frenklach, M. Goldenberg, G.P. Smith, D.R. Crosley, D.M. Golden, Technical Report Gaz Research Institute Chicago, IL, Report No. GRI-97/0020, 1997.
[37] V. Robin, A. Mura, M. Champion, Proceedings of the XXIst International Colloquium on the Dynamics of Explosions and Reactive Systems (ICDERS), Poitiers, France, 2007, submitted for publication.
[38] G. Ribert, M. Champion, O. Gicquel, N. Darabiha, D. Veynante, Combust. Flame 141 (3) (2005) 271–280.
[39] M.S. Anand, S.B. Pope, Combust. Flame 67 (1987) 127–142.
[40] P.A. Libby, K.N.C. Bray, Combust. Flame 39 (1) (1980) 33–41.
[41] T. Mantel, R. Borghi, Combust. Flame 96 (1994) (1980) 443–447.
[42] A. Mura, R. Borghi, Combust. Flame 133 (2003) 193–196.
[43] N. Swaminathan, K.N.C. Bray, Combust. Flame 143 (4) (2005) 549–565.
[44] A. Mura, V. Robin, M. Champion, Combust. Flame 149 (2007) 217–224.
[45] R. Borghi, in: C. Casci (Ed.), Recent Advances in the Aerospaces Sciences, Plenum Publishing Corporation, 1985, pp. 117–138.
[46] F. Archambeau, N. Mehitoua, M. Sakiz, Int. J. Finite Volumes (2004), http://averoes.math.univ-paris13.fr/IJFV/.
[47] J.B. Bell, M.S. Day, L.G. Shepherd, M.R. Johnson, R.K. Cheng, J.F. Grcar, V.E. Beckner, M.J. Lijewski, Proc. Natl. Acad. Sci. 102 (29) (2005) 10006–10011.
[48] N. Peters, Turbulent Combustion, Cambridge Univ. Press, Cambridge, 2000.